Delineating the pathway that leads to aneuploidy-induced senescence

Jery Joy[1], Lara Barrio[1], Celia Santos-Tapia[1], Daniela Romão[1], Nikolaos Nikiforos Giakoumakis[1], Marta Clemente[1], and Marco Milán[1,2,3] *

[1] Institute for Research in Biomedicine (IRB Barcelona), The Barcelona Institute of Science and Technology, Baldiri Reixac, 10, 08028 Barcelona, Spain.

[2]Institució Catalana de Recerca i Estudis Avançats (ICREA)

Pg. Lluís Companys 23, 08010 Barcelona, Spain

[3]Lead Contact

* Correspondence: marco.milan@irbbarcelona.org

Phone/Fax: 34 93 4034902/34 93 4037109

Running title: CIN-induced senescence

Keywords: *Drosophila*, aneuploidy, proteotoxic stress, mitochondrial dysfunction, tissue repair

Number of figures: 7

(+ 7 supplementary figures, 8 supplementary videos and 2 supplementary tables)

Number of characters: 50571 (with spaces)

Summary

Aneuploidy, an unbalanced number of chromosomes, is highly deleterious at the cellular level and leads to senescence, a stress-induced response characterized by permanent cell cycle arrest and a well-defined associated secretory phenotype. Here we use a *Drosophila* epithelial model to delineate the pathway that leads to the induction of senescence as a consequence of the acquisition of an aneuploid karyotype. Whereas aneuploidy induces, as a result of gene dosage imbalance, proteotoxic stress and activation of the major protein quality control mechanisms, near-saturation functioning of autophagy leads to compromised mitophagy, accumulation of dysfunctional mitochondria and the production of radical oxygen species (ROS). We uncovered a role of JNK in driving senescence as a consequence of dysfunctional mitochondria and ROS. We show that activation of the major protein-quality control mechanisms and mitophagy dampen the deleterious effects of aneuploidy and identify a role of senescence in proteostasis and compensatory proliferation for tissue repair.

Introduction

Chromosomal Instability (CIN), an increased rate of changes in chromosome structure and number, is a hallmark of most solid tumors of epithelial origin. CIN contributes to the gain of chromosomes carrying oncogenes and the loss of those carrying tumor suppressor genes (Ben-David and Amon, 2020). However, the impact of CIN on the biology of the cell, on the homeostasis of the tissue and on the fitness of the organism are far from being fully elucidated. Of note are the highly deleterious effects of CIN as a result of the generation of highly aneuploid karyotypes. Work in yeast and human cells has shown that an unbalanced number of chromosomes leads to altered protein stoichiometry and impaired functioning of large protein complexes involved in replication, mitosis, and metabolism (Santaguida and Amon, 2015; Zhu et al., 2018). One of the consequences of metabolic stress is the production of radical oxygen species (ROS). Ultimately, highly aneuploid cells enter a state of senescence, characterized by permanent cell cycle arrest and an enhanced secretory phenotype (Barroso- Vilares et al., 2020; Macedo et al., 2018). The production of pro-inflammatory cytokines has been proposed to contribute to the elimination of these cells by the immune system (Santaguida et al., 2017). To date, the molecular mechanisms driving aneuploidy-induced senescence and its potential contribution to tissue repair and tumorigenesis have not been elucidated.

The *Drosophila* wing primordium has proved a useful model system to identify the relevant cell populations and pertinent cell interactions involved in the response of an epithelial tissue to CIN, and to functionally decipher the molecular mechanisms driving emerging, tumor-like cellular behaviors (Dekanty et al., 2012; Milán et al., 2014; Morais da Silva et al., 2013). In this model, cells with highly aneuploid karyotypes delaminate as a result of chromosome-wide gene dosage imbalances and the production of ROS (Clemente-Ruiz et al., 2016). ROS contribute to activating the stress JNK signaling pathway through Ask1 (Muzzopappa et al., 2017), and JNK induces the transcriptional activation of pro-apoptotic genes and the death of these cells. Upon apoptosis inhibition, CIN tissues produce tumor-like overgrowths that grow extensively and metastasize in allograft transplantations (Dekanty et al., 2012). This tumorigenic response relies on JNK, which remains strongly activated in highly aneuploid cells that delaminate from the epithelium. JNK activates a transcriptional program that drives non-autonomous tissue overgrowth through the expression of mitogenic molecules, basement membrane degradation through the expression of MMPs, and tissue invasiveness by modulating the actin-myosin cytoskeleton (Benhra et al., 2018). Cross-feeding interactions between delaminating cells

producing mitogenic molecules and epithelial cells acting as source of new aneuploid cells are responsible for the unlimited growth potential of CIN-tumors (Muzzopappa et al., 2017). Remarkably, many of the molecular responses and cellular and tissue-wide behaviors identified in the fly epithelial model of CIN, such as ROS production, extrusion of aneuploid cells, metastatic behavior, expression of pro-inflammatory signals and tumorigenesis, have been also observed in mammalian epithelial tissues subjected to CIN (Bakhoum et al., 2018; Levine et al., 2017; Li et al., 2010; Rowald et al., 2016; Santaguida et al., 2017).

Using the fly model of CIN, we present evidence that upon apoptosis inhibition highly aneuploid cells enter a state of senescence, characterized by permanent cell cycle arrest in G2 and an enhanced secretory phenotype. We delineate the pathway that leads to senescence as a response to aneuploidy. We first show that aneuploidy-induced proteotoxic stress, as a result of gene dosage imbalances, and near-saturation of autophagy contribute to impaired mitophagy. The resulting accumulation of dysfunctional mitochondria and the production of ROS contribute to activating a cellular program in aneuploid cells that drives JNK-driven senescence. Lastly, we unravel a role of aneuploidy-induced senescence in proteostasis and compensatory proliferation and demonstrate that activation of the major protein quality control mechanisms and mitophagy dampens the deleterious effects of aneuploidy.

Results

The ubiquitin-proteasome system is functioning near-saturation in CIN tissues

The wing primordium of *Drosophila* is a highly proliferative monolayer epithelium (Figure 1A, A'). RNAi-mediated depletion of the spindle assembly checkpoint (SAC) gene *rod* in this tissue induces high levels of CIN, and the resulting aneuploid cells delaminate basally from the epithelium, activate JNK and die (Figure 1C). To maintain aneuploid cells in the tissue, we co-expressed the baculovirus caspase inhibitor *p35* (Hay et al., 1994), or a synthetic miRNA that targets the pro-apoptotic genes *reaper*, *hid* and *grim* [miRHG, (Siegrist et al., 2010)]. We targeted the expression of these transgenes to the posterior compartment of the wing, while the anterior compartment acted as a control tissue (Figure 1B). The highly aneuploid delaminated population, marked with a cyan line from here onwards, was located on the basal side of the epithelium, and cells were loosely attached and expressed the JNK target MMP1 (Figure 1B' and Figure S1A). Morphological differences and MMP1 staining (which was removed from most images to simplify them) were used to identify the highly aneuploid delaminated population. The ubiquitin-proteasome system (UPS) plays a crucial role in governing normal protein turnover and protein quality control by degrading misfolded and damaged proteins, and protein ubiquitylation serves as an essential degradation signal for proteins. CIN-tissues showed evidence of proteotoxic stress, as monitored by the presence of poly-ubiquitin (Ubq) aggregates (Figure 1D). These aggregates were also positive for the ubiquitin receptor p62 [Ref(2)P in flies (Nezis et al., 2008)]. Ubq- and Ref(2)P-positive aggregates were observed mainly in the P compartment, specifically in delaminated cells (Figure 1E, E'). Similar aggregates were observed in delaminated cells of wing discs upon depletion of the SAC gene *bub3* or the spindle assembly gene *asp* (Figure S1A-B), experimental conditions that induce high levels of CIN (Dekanty et al., 2012). To further address whether protein aggregates appeared in CIN-induced aneuploid cells, we used Htt25Q, a fusion protein consisting of human Huntingtin with a polyQ stretch containing only 25 glutamines and fused to a Cerulean fluorescent protein (Ramdzan et al., 2017). Htt25Q does not form aggregates nor does it cause toxicity on its own but the existence of protein aggregates in the cell can seed Htt25Q polymerization (Serpionov et al., 2016). Whereas Htt25Q showed diffused expression in control wing discs, Htt25Q was accumulated in big foci upon CIN and mostly in delaminating cells (Figure 1F-G'), thus pointing to the appearance of protein aggregates in these cells.

The Male-Specific Lethal complex (MSLc) targets X-chromosomes in males to increase gene transcription to a similar level to that observed in autosomal chromosomes (Lucchesi and Kuroda, 2015). Upon depletion of the MSLc, male tissues fail to increase the transcription of this chromosome, thus causing a chromosome-wide gene expression imbalance of the X-chromosome with respect to autosomes that can be used to assess whether these imbalances phenocopy the cellular stresses that occur in aneuploid cells (Clemente-Ruiz et al., 2016). Depletion of the MSL-C gene *msl-1* in male tissues expressing p35 gave rise to the appearance of Ref(2)P-positive aggregates (Figure S1A, A', B). Planar polarization of the mitotic spindle in the wing epithelium is oriented by the dynein/dynactin motor complex, whose cortical localization depends on Mud/NUMA (Nakajima et al., 2013). Failure of the mitotic spindle to achieve planar polarization induces cell delamination. In contrast to CIN-tissues, the DNA content profile of delaminated cells in *mud*-depleted tissues did not reveal a high percentage of cells with DNA content higher than 4C (Figure S6E, F). Thus, the behavior of these cells can be used to assess whether delamination per se phenocopies the cellular stresses that occur in CIN-induced aneuploid cells. Interestingly, Ref(2)P-positive aggregates were not observed in *mud*-depleted tissues (Figure S1A, A', B). These results imply that these aggregates are an outcome of CIN-induced aneuploidy and the associated gene dosage imbalance, and not a trivial consequence of cell delamination.

The proteasome is a multi-subunit protease complex (de Poot et al., 2017). To characterize the *in vivo* activity of the proteasome in CIN tissues, we used CL1-GFP, a fusion protein created by attaching a proteasome degradation signal to GFP (Pandey et al., 2007). Whereas CL1-GFP was rapidly degraded in control wing discs and no accumulation was observed, it was accumulated upon CIN and mostly in delaminating cells, where it co-localized with Ubq-positive aggregates (Figure 1H-J). These data suggest that the proteasome is near saturation in CIN-induced aneuploid cells. In order to reinforce this proposal, we selected a number of RNAis against various proteasome subunits (Rpn) that did not have phenotypic consequences in terms of tissue size when expressed in otherwise *wild-type* eyes (Figure 1K, bottom panels), and we tested their ability to enhance the deleterious effects of CIN. Similar to the wing, the eye primordium is a highly proliferative monolayer epithelium. Induction of CIN with an eye-specific Gal4 (*eyeless-gal4*) driving *bub3*-RNAi expression caused cell death in the eye primordium and produced rough eyes with a reproducible mild reduction in size (Figure 1K, Figure S1C, Table S1). Upon apoptosis inhibition, highly aneuploid cells remained in the basal side of the eye epithelium, activated JNK and accumulated CL1-GFP (Figure S1D-F).

Interestingly, co-depletion of *bub3* and several *rpn* genes resulted in strongly reduced adult eyes (Figure 1K, upper panels). Co-expression of HttQ25 gave similar results and increased the number of apoptotic cells observed in CIN tissues (Figure 1K, Figure S1G, I). Usp14 is a deubiquitinating enzyme identified as an endogenous inhibitor of the proteasome (Hanna et al., 2006), and mutations in Usp14 improve the fitness of aneuploid yeast cells (Torres et al., 2010). Depletion of *usp14* rescued the size of eyes subjected to CIN and the number of apoptotic cells observed in CIN tissues (Figure 1K, Figure S1G, H). These data indicate that the UPS is working near saturation in tissues subject to CIN and that experimental activation of the UPS can dampen the deleterious effects of CIN.

Autophagy induction and flux play critical roles in CIN tissues

Together with the UPS, autophagy - a pathway responsible for the lysosomal degradation of cellular components - plays an essential role in maintaining protein homeostasis (proteostasis). p62 [Ref(2)P in flies, (Nezis et al., 2008)], acts as a receptor of ubiquitinated proteins and binds to Atg8, which becomes membrane-associated under autophagy induction and localizes to the site of autophagosome nucleation. The observed accumulation of Ref(2)P-positive aggregates in CIN-induced aneuploid cells suggests that autophagic degradation is either saturated or not functioning. We thus analyzed whether autophagy induction, its flux, and lysosomal biogenesis were functioning in these cells. High levels of autophagy were induced in CIN tissues expressing p35 or miRHG, as visualized by the punctated accumulation of ChAtg8a (a mCherry-tagged form of Atg8a) and this induction was more prevalent in delaminated cells (Figure 2A-C', Figure S2G). Autophagy was also elevated in the anterior compartment, where CIN cells are not present. This non-autonomous induction of autophagy resembles the one caused by oncogene-driven fly epithelial tumors (Katheder et al., 2017). ChAtg8a-positive puncta were observed also in delaminated cells of *bub3*- or *asp*-depleted wing and eye discs, but not in *mud*-depleted tissues (Figure S2G). We noticed that many of the Ref(2)-positive aggregates did not co-localize with ChAtg8a-positive puncta (Figure 2D, E, E'), pointing to the pathological accumulation of autophagic cargo. Induction of autophagy depended on the presence of the cargo and the activity of Atg1, as autophagy levels were reduced in CIN tissues expressing *ref(2)P*- or *atg1-RNAi* (Figure 2G, G', K, Figure S2B). In *atg1*-depleted tissues, the density of Ref(2)P- and Ubq-positive aggregates and the extent of CL1-GFP accumulation increased dramatically (compare Figure 2H-K and Figure 1D, I, see also

Figure S2A). Importantly, Ref(2)P-positive aggregates were now observed in epithelial cells (Figure 2I, I', arrowheads, compare with Figure 1E, E'). These findings indicate that autophagy is functioning in CIN tissues near saturation. To reinforce this proposal, we tested several RNAis against different *atg* genes for their ability to enhance the CIN-induced deleterious effects. Whereas depletion of *atg* genes did not have any overt consequence in adult eyes or epithelial tissues of otherwise *wild type* individuals, it reduced the size of eyes subjected to CIN and increased the number of CIN-induced apoptotic cells (Figure 2F, Figure S2C-E). Overexpression of Ref(2)P, known to boost autophagy (Aparicio et al., 2019), rescued both eye size and number of apoptotic cells caused by CIN (Figure 2F, Figure S2F). Thus, autophagy is working near saturation in CIN tissues and experimental activation of autophagy can dampen the deleterious effects of CIN.

We next used the tandem tagged mCherry-GFP-Atg8a reporter to study autophagic flux. The low lysosomal pH rapidly quenches the GFP signal after fusion and the autophagolysosome is only positive for mCherry. In CIN-induced tissues, most Atg8a-positive puncta were located in delaminated cells and were positive for mCherry only (Figure 3A, A', D). However, some large puncta positive for both signals were observed in delaminating cells. Depletion of Syntaxin17 [Syx17, a protein required for lysosomal fusion (Takáts et al., 2013)] resulted in an accumulation of puncta positive for both signals and these puncta could now be observed not only in delaminated cells but also in cells that remained in the epithelium (Figure 3B, B', D). No major effect on autophagy flux was observed upon Syx17 depletion in control tissues (Figure S3A-B). In *Drosophila*, Mitf, the single ortholog of TFEB and MITF (microphthalmia-associated transcription factor), coordinates lysosome biogenesis (Bouché et al., 2016; Tognon et al., 2016; Zhang et al., 2015). Mitf expression and activity (monitored by the Mitf-2.2-GFP transcriptional reporter and the Mitf synthetic target 4Mbox-GFP) were both induced in CIN-tissues and this induction was more prevalent in delaminated cells (Figure 3E-H). Consistently, these cells were positive for Lysotracker Red (LTR), which labels acidic organelles such as lysosomes, and for a tagged version of Lysosomal-associated membrane protein 1 (LAMP1, Figure 3I-L, Figure S3F). As it occurs with autophagy, some cells of the nearby anterior compartment not subjected to CIN and some cells subjected to CIN that remained in the epithelium were positive for LTR and induced Mitf (Figure 3E-J). Interestingly, autophagy flux was reduced in CIN tissues subjected to Mitf-depletion (Figure 3C, D). By contrast, levels of autophagy induction were only slightly reduced under these conditions (Figure S3C). To sum up, autophagy flux is functioning in CIN-induced tissues. However, the accumulation of autophagic cargo

and presence of few yellow dots suggests that this flux is close to saturation. Consistent with this proposal, depletion of *syx17* or *mitf* reduced the size of eyes subjected to CIN and increased the number of CIN-induced apoptotic cells (Figure 3M, N). Depletion of *syx17* or *mitf* in otherwise *wild-type* tissues had no major impact on eye size or cell death (Figure 3M, Figure S3D). Overexpression of Spinster [Spin, a protein involved in autolysosome formation in flies and vertebrates (Rong et al., 2011; Sasaki et al., 2017)] rescued the size of eyes subjected to CIN (Figure 3M). These data indicate that autophagy flux is working near saturation in tissues subject to CIN and that experimental induction of autolysosome formation can dampen the deleterious effects of CIN.

UPR, HIF and TOR regulate autophagy in aneuploid cells

Autophagy can be induced by different means in a highly pleiotropic condition such as CIN. The Unfolded Protein Response (UPR), inhibition of the UPS and the resulting reduction in the amino acid pool are all well known to be involved in triggering autophagy (He and Klionsky, 2009). We thus tested whether the corresponding sensing pathways are activated upon CIN and whether they play a role in autophagy induction.

In normoxia, Hypoxia-Inducible transcription Factor-1 (HIF-1, known as Sima in *Drosophila*) is degraded by the UPS (Lavista-Llanos et al., 2002). Upon hypoxia or UPS inhibition, HIF-1 is not degraded, induces expression of Lactate dehydrogenase (LDH, a key enzyme involved in anaerobic metabolism) and activates autophagy (Lőw et al., 2013). Sima and LDH levels and those of the Sima biosensor ODD-GFP (Misra et al., 2017) were highly increased in CIN tissues, especially in delaminated cells (Figure 4A, B, B'). Sima activation was not a result of hypoxia, as shown by the oxygen biosensor nlsDsRedFT [Figure S4A, B, (Lidsky et al., 2018)] and was most probably caused by UPS saturation (Lőw et al., 2013). Interestingly, depletion of *sima* in CIN-tissues reduced the extent of autophagy induction (Figure 4H-I', N, Figure S4C, D).

Target of Rapamycin (TOR) plays a vital role in nutrient sensing and autophagy regulation. During nutrient availability, TOR represses Atg1 through direct phosphorylation (Noda and Ohsumi, 1998). Amino acid pools are maintained by proteasome-dependent degradation, and UPS inhibition reduces TOR activity and triggers autophagy as a compensatory mechanism to replenish the amino acid pool (Suraweera et al., 2012). TOR regulates transcription by inhibiting the nuclear localization of the REPTOR transcription factor (Tiebe et al., 2015). High levels of the REPTOR transcriptional reporter *unk-GFP* were observed in CIN-induced tissues,

especially in delaminated cells (Figure 4C-D'). These results together with the observed induction of autophagy (Figures 2A-C, 3E-H) indicate that TOR is repressed in CIN-induced aneuploid cells. Consistently, overexpression of the small GTPase Rheb to activate TOR lowered the degree of autophagy induction and *unk-GFP* expression (Figures 4J, J', N, Figure S4J). TOR activation also increased the accumulation of Ref(2)-positive aggregates in CIN tissues and enhanced the CIN-induced eye phenotype (Figure 4G, Figure S4F-I), supporting the proposal that autophagy induction and flux counteract the deleterious effects of CIN and that they are functioning near saturation in these tissues. We would like to note, though, that other downstream effectors besides autophagy might also contribute to the negative impact of TOR activation in CIN tissues.

The UPR is activated in response to accumulation of unfolded or misfolded proteins in the lumen of the endoplasmic reticulum (ER), thereby leading to the halting of protein translation, the degradation of misfolded proteins, and increased production of molecular chaperones involved in protein folding. Three UPR sensors are embedded in the ER membrane: (1) PERK (protein kinase RNA-like endoplasmic reticulum kinase), which phosphorylates eIF2α (eukaryotic Initiation Factor 2) to inhibit global protein synthesis and induce selective translation of Activating Transcription Factor 4 (ATF4); (2) ATF6 (activating transcription factor 6), whose cleaved form translocates to the nucleus; and (3) IRE1 (inositol-requiring enzyme 1), which activates, through splicing, the XBP1 (X-box binding protein 1) transcription factor. Levels of phosphorylated eIF2α and the spliced form of XBP1-GFP (Ryoo et al., 2007) were both upregulated in CIN tissues, especially in the highly aneuploid delaminated cells (Figure 4E, F, F', Figure S4E), indicating that the UPR is activated in this population. It is well known that UPR sensors and transcriptional mediators are also upregulated upon UPR activation. Consistently, we found increased expression of PERK, ATF4 and ATF6 in CIN tissues (Figure S4K, K'). Importantly, depletion of *perk*, *ire1* or *xbp1* lowered autophagy induction in CIN tissues (Figure 4L-N). BiP (Hsc70-3 in *Drosophila*) is both mediator and transcriptional target of the UPR and encodes for an ER-resident chaperone with a critical role in the clearance of misfolded ER aggregates and degradation of membrane-associated proteins (Gething, 1999). BiP depletion enhanced the CIN-induced eye phenotype and increased the number of CIN-induced apoptotic cells (Figure 4G, O, Figure S4L). Depletion of *sip3* (*septin interacting protein 3*), which promotes the degradation of misfolded peptides in the ER, gave similar results and induced an accumulation of Ref(2)-positive aggregates (Figure 4G, H, O, Figure S4M-O). By contrast, overexpression of BiP rescued the size of eyes subjected to CIN and reduced the number of CIN-induced apoptotic cells

(Figure 4G, O, Figure S4L). All together, these results indicate that autophagy is induced by at least three distinct mechanisms in a highly pleiotropic condition such as CIN. We can also conclude that experimental increase in the degradation of misfolded ER aggregates by means of BiP overexpression can dampen the deleterious effects of CIN.

Mitochondrial dysfunction in aneuploid cells contributes to ROS production

Selective autophagy of mitochondria, known as mitophagy, is an important quality control mechanism that eliminates damaged mitochondria. We reasoned that near saturation of autophagy and its flux might compromise mitophagic activity thus leading to the accumulation of dysfunctional mitochondria in CIN-induced aneuploid cells. *Wild-type* cells are decorated by a highly filamentous array of mitochondria (Figure 5A-A'', Video S1). By contrast, fragmented mitochondria were accumulated in CIN tissues, and this accumulation was more prominent in delaminated cells (Figure 5B-B'',D, Video S2). Transmission electron microscopy (TEM) and expansion microscopy of CIN-tissues confirmed the presence of fragmented mitochondria in CIN-induced delaminated cells (Figure 5C, Figure S5G,H). We then used the MitoTimer reporter, which targets the oxidation-sensitive Timer protein to mitochondria (Laker et al., 2014). The shift of mitochondrial fluorescence toward red observed in CIN-induced aneuploid cells (compare Figure 5E, E'' and Figure 5F, F'') pointed either to high rates of mitochondria oxidation or to slow rates of mitochondria turnover. The ER is a major storehouse of calcium (Ca^{2+}), which is released to the cytoplasm upon stress. Upon ER stress, attached organelles like mitochondria can experience a heavy Ca^{2+} influx that drives mitochondria fragmentation and dysfunction and the production of ROS. Interestingly, two genetically encoded Ca^{2+} indicators revealed increased Ca^{2+} levels in the cytoplasm (GCaMP) and mitochondria (Mito-GCaMP) of CIN tissues (Figure S5A-D'). Mitochondrial membrane potential generated by proton pumps is an essential component in the process of energy storage during oxidative phosphorylation. In CIN-induced aneuploid cells, mitochondria were either depolarized or hyperpolarized, reinforcing the proposal that mitochondria are dysfunctional (Figure S5E-F'). The presence of dysfunctional mitochondria prompted us to look for mitochondria positive for autophagy markers. Fragmented and accumulated mitochondria present in the tissue were positive for the autophagy adaptor Ref(2)P (arrows in Figure 5G, Pearson's correlation coefficient for signal colocalization was 0,74, n=9 wing discs), and super-resolution microscopy analysis revealed that many of the large autophagic cargoes (61,5%; n=65) colocalized

with fragmented mitochondria (arrows in Figure 5H, H', Figure S5I, Videos S3, S4). Targeting of damaged mitochondria to mitophagy relies on the activity of PINK1 (PTEN-induced putative kinase 1), a mitochondrially localized kinase that phosphorylates Ubiquitin and Parkin upon loss of mitochondria membrane potential. The E3-ligase activity of Parkin is enhanced upon phosphorylation, thus placing more ubiquitin for successive phosphorylation. Mitochondria labeled with phospho-ubiquitin-chains are recognized by the autophagic adaptor, which results in autophagosome formation. We then used MitoQC (Lee et al., 2018), where a tandem GFP-mCherry fusion protein is targeted to the outer mitochondria membrane, to analyze mitophagy in CIN tissues. MitoQC exploits the pH sensitivity of GFP to enable the differential labeling of mitochondria in the acidic microenvironment of the lysosome as a proxy endpoint readout. Only a few small MitoQC-positive puncta, most of them red, marking mitolysosomes, were observed in *wild-type* tissues (arrows in Figure 5I-I'',P). By contrast, the number of MitoQC-positive puncta was very high in CIN tissues, and many of them were positive for both colors and of small (arrowheads) and large size (asterisks, Figure 5J-N', P, Figure S5K, Video S5). Similar results were obtained with the mitophagy reporter MitoKeima (Figure S5L). Structural illumination microscopy (SIM) and expansion microscopy analysis unraveled that the large MitoQC-positive aggregates consisted of tens of mitochondria and co-localized with lysosomes (Figure 5M-N', Figure S5J, K, N, Video S6). Few red-only dots (arrows) were also found. Increased number of MitoQC-positive puncta were also observed in CIN-induced delaminated cells of *asp*-depleted tissues or when apoptosis was blocked by expressing miRHG in *rod*-depleted tissues (Figure S5M). Correlative light electron microscopy (CLEM) of CIN tissues confirmed the subcellular localization of red MitoQC-positive puncta to lysosomes (arrows in Figure 5O and zoom of the same area in Figure S5 P.1) and unraveled the accumulation of yellow MitoQC-positive mitochondria not only in the cytoplasm of delaminated cells (arrowhead in Figure 5O and Figure S5 P.4) but also in extracellular vesicles (Figure S5 P.2, Figure S5 P.3). This latter observation suggests that aneuploid cells, as previously observed in mesenchymal stem cells (Phinney et al., 2015), might remove unwanted mitochondria through their release into the extracellular compartment via specialized vesicles (Figure S5 P.2, Figure S5 P.3). Taken together, these results indicate that mitochondria are highly dysfunctional in CIN-induced aneuploid cells and that mitophagy is highly saturated in these cells. Eye primordia subjected to CIN also showed a high number of MitoQC-positive puncta and large mitochondrial aggregates positive for both colors in the basal side of the epithelium (Figure S5O). Several RNAis against different genes involved in

mitochondria homeostasis or mitophagy, including *parkin*, enhanced the CIN-induced eye phenotype and the number of apoptotic cells but did not have phenotypic consequences in terms of tissue size when expressed in otherwise *wild-type* eyes (Figure 5Q, R, Figure S5R, S). By contrast, upregulation of Parkin, known to activate mitophagy in fly tissues (Rana et al., 2013), rescued the CIN-induced eye phenotype and the number of CIN-induced apoptotic cells (Figure 5Q, R, Figure S5S). Similar results were obtained upon overexpression of mitochondria-specific chaperones Hsp60 and Hsp60c or ROS scavengers Sod2, GTPx-1 and CatA (Figure 5Q). Three separate observations indicate that ROS are induced, at least in part, by near-saturation of mitophagy and the resulting mitochondrial dysfunction. First, both cytoplasmic and mitochondrial ROS were observed in CIN-induced aneuploid cells [Figure 5S-U, (Clemente-Ruiz et al., 2016)]. Second, ROS levels were increased upon depletion of *atg9* or *mitf* (Figure 5V, Figure S5U). Third, the levels of mitochondrial ROS were rescued by Ref(2)P or Parkin overexpression, or *usp-14* depletion (Figure 5W), all these experimental conditions well known to activate mitophagy (Aparicio et al., 2019; Chakraborty et al., 2018). Altogether, our data indicate that experimental depletion of ROS, either by overexpressing ROS scavengers and mitochondria chaperones or by inducing mitophagy, can dampen the deleterious effects of CIN.

A role of JNK in aneuploidy-induced senescence, proteostasis and compensatory proliferation

We observed that CIN-induced aneuploid cells presented features of senescence, a state of stable cell cycle arrest characterized by morphological and metabolic changes, altered gene expression, ER stress, accumulation of dysfunctional mitochondria, increased lysosomal content and adoption of a pro-inflammatory phenotype known as the senescence-associated secretory phenotype (SASP, (Hernandez-Segura et al., 2018)). These cells express many secreted molecules, including mitogenic molecules, cytokines, EGFR ligands, Matrix Metalloproteinases, the systemic hormone Dilp8, and the non-functional secreted protease Scarface [Figure S6A, (Benhra et al., 2018; Clemente-Ruiz et al., 2016; Dekanty et al., 2012; Muzzopappa et al., 2017)]. Consistently, the ER and Golgi apparatus were enlarged (Figure S6B, C). These cells were also mitotically inactive, as monitored by the lack of pH3 staining and EdU incorporation (Figure 6A-C), and presented an enlarged cellular and nuclear size (Figure 6E, F, Figure S6E). To address whether these cells were arrested in G1 or G2, we used Fly-Fucci, which relies on fluorochrome-tagged degrons from the Cyclin B (in red) and E2F1 (in green) proteins that are degraded in mitosis or at the onset of the S phase, respectively

(Zielke et al., 2014). The percentage of delaminated cells in G2 was increased and the percentage of cells in G1 was correspondingly reduced (Figure 6D). DNA content analysis of FACS-sorted dissociated wing disc cells showed an accumulation of delaminated cells during the G2/M phases (Figure S6D, E). The behavior of *mud*-depleted misaligned cells can be used to assess whether delamination phenocopies the cell cycle arrest observed in CIN-induced aneuploid cells. Delaminated cells observed in *mud*-depleted tissues accumulated in G2/M but were mitotically active (Figure S6F, G). Cell cycle arrest in senescent mammalian cells relies on p53 activity and the transcriptional induction of p21/p27, which blocks cell cycle arrest in G1 (Gorgoulis et al., 2019). Although *Drosophila* orthologues of p53 (*Dp53*) and p21/p27 (*Dacapo*) were induced in CIN tissues, they did not participate in the cell cycle arrest (Figure S6K-N). By contrast, JNK activation played a key role not only in the cell cycle arrest in G2, but also in the increase in nuclear and cellular size (Figure 6A-F). The senescence-associated β-galactosidase (SA-β-Gal) assay is the most widely used test to detect senescent cells. CIN tissues were positive for SA-β-Gal, the staining was more prominent in the delaminated population, and depletion of the JNK pathway rescued the increased levels of SA-β-Gal (Figure 6G). CIN tissues also showed high levels of DNA damage, and aneuploid cells activated the DNA damage response pathway and presented enhanced levels of the heterochromatin protein HP1 (Figure S6H-J). All these results indicate that CIN-induced delaminated cells enter a JNK-driven senescent state.

Despite the levels of apoptosis observed in CIN tissues, their impact on the size of adult structures [wings, (Dekanty et al., 2012) and eyes, Figure 7A] was mild. These observations suggest that epithelial primordia give rise to nearly normal-looking adult structures as a result of compensatory proliferation (Haynie and Bryant, 1977). Consistently, in CIN tissues in which apoptotic was not inhibited, mitotic activity in the epithelium was clearly increased when compared to *wild-type* controls (Figure 7B, C). We next addressed whether JNK-driven senescence and its associated SASP contribute to the observed increase in mitotic activity in CIN tissues and to tissue repair. Whereas JNK blockage did not have major phenotypic consequences in terms of mitotic activity or tissue size when expressed in otherwise *wild-type* eyes, it reduced the mitotic activity of CIN tissues and enhanced the CIN-induced eye phenotype (Figure 7A-C). Tissue size reduction was also observed in developing wing primordia subjected to CIN and depleted for JNK (Figure 7B, C). We noticed that similar to the wing epithelium, the eye epithelium subjected to CIN was positive for SA-β-Gal and induced the expression of mitogenic molecules (Figure S7A) whose depletion also enhances the CIN-induced eye phenotype

(Clemente-Ruiz et al., 2016). Interestingly, we observed that JNK depletion in CIN-induced aneuploid cells also reduced the levels of autophagy induction and lysosomal biogenesis, and increased the number of Ref(2)P-positive aggregates and the accumulation of CL1-GFP (Figure 7D-G', Figure S7A-A´). These results unravel roles of JNK-driven senescence in compensatory proliferation for tissue repair, most probably through the production of mitogenic molecules, and in dampening the deleterious effects of aneuploidy by activating the major protein quality control mechanisms. Autophagy induction by JNK could be direct (Wu et al., 2009). However, JNK is also well known to drive the expression of IL-6-like Unpaired cytokines in CIN-induced aneuploid cells (Clemente-Ruiz et al., 2016). Interestingly, blocking the JAK-STAT pathway by expressing a dominant negative version of Domeless lowered autophagy induction levels in CIN tissues indicating that JAK/STAT could also contribute to autophagy induction downstream of JNK (Figure 7D-D´, Figure S7A-A´).

Discussion

A central role of autophagy in antagonizing proteotoxic stress in CIN tissues

In yeast and mammals, aneuploidy generates, as a result of gene dosage imbalance, proteotoxic stress and activates autophagy as the major quality control mechanism aimed at maintaining proteostasis (Santaguida et al., 2015; Stingele et al., 2013). To delineate the cascade of events that lead to the induction of autophagy as a result of aneuploidy, we used a *Drosophila* epithelial model of CIN (Benhra et al., 2018; Clemente-Ruiz et al., 2014, 2016; Dekanty et al., 2012; Morais da Silva et al., 2013; Muzzopappa et al., 2017) that recapitulates most emerging cellular behaviors observed in mammalian epithelial tissues upon CIN, such as extrusion of aneuploid cells, invasive behavior, expression of pro-inflammatory signals and tumorigenesis (Bakhoum et al., 2018; Levine et al., 2017; Rowald et al., 2016; Santaguida et al., 2017). We present evidence that epithelial cells with high levels of aneuploidy show strong levels of proteotoxic stress and that the proteasome is functioning near saturation (Figure 7H). In this context, it is interesting to speculate that aneuploidy might have a direct impact on the stoichiometry of the proteasome, thus further compromising its activity. In addition to p62-mediated autophagy, we identified three distinct molecular mechanisms by which autophagy is triggered in aneuploid cells. Repression of TOR and activation of HIF, most probably caused by proteasome malfunction, and activation of UPR contributes to autophagy induction. In addition, Mitf/TFEB activation contributes to lysosomal biogenesis. As occurs with the proteasome, our data also indicate that autophagic induction and

flux are functioning near saturation. As a consequence, mitophagy is compromised thus leading to the accumulation of dysfunctional mitochondria. Consistently, we observed that reducing the levels of autophagy or the activity of those pathways mediating autophagy induction increased the levels of mitochondrial ROS observed in CIN tissues (Figure S7F). Despite the highly pleiotropic effects of CIN and aneuploidy, our work has demonstrated that experimental activation of the major protein quality mechanisms (by targeting the deubiquitinating enzyme USP14 or overexpressing Ref(2)P/p62, Spin or the ER chaperon BiP) or induction of mitophagy (by overexpressing Parkin) can have a profound effect in dampening the deleterious effects of CIN on the tissue. All these results open new avenues towards the use of chemical therapy to dampen aneuploidy-associated cellular stresses and target most solid tumors of epithelial origin, characterized by high levels of aneuploidy.

Mitochondria as sensing and signaling organelles in aneuploid cells

Research in the last two decades has provided evidence that mitochondria function as signaling organelles, communicating with the cytosol to initiate biological processes under homeostatic and stress conditions (Chandel, 2014). In CIN tissues, a dysfunctional pool of mitochondria was present. Beside mitophagy saturation, mitochondria per se may be affected by proteotoxic stress. Indeed, mitochondria contain more than 1000 different proteins, which are imported from the cytoplasm through the TOM complex (Mokranjac, 2020), and various defects, including excessive ROS, impaired complex assembly or accumulation of misfolded proteins, impair the efficiency of mitochondrial protein import and activate the mitochondrial UPR [mtUPR, (Shpilka and Haynes, 2018)] to enhance the repair and recovery of the mitochondrial network. Similar to the role of ATFS-1 in worms and ATF5 in mice in mediating the mtUPR, PGAM5 mediates the mtUPR response in *Drosophila* by activating JNK to enhance the transcription of mitochondrial chaperones (Borch Jensen et al., 2017; Owusu-Ansah et al., 2013). Depletion of PGAM5 reduced the activity levels of JNK (Figure S7B) and the number of apoptotic cells in CIN tissues (Figure S7C, D), and enhanced the CIN-induced eye phenotype (Figure 7A). By contrast, overexpression of mitochondrial chaperones rescued the CIN-induced eye phenotype (Figure 5J). Thus, mitochondria activate JNK not only through the production of ROS, as previously reported (Clemente-Ruiz et al., 2016), but also through the activity of PGAM5. Interestingly, the JNKK kinase Ask1, which is activated by ROS through its binding to Thioredoxin (Sekine et al., 2012) and by

PGAM5 through dephosphorylation of inhibitory sites (Takeda et al., 2009), mediates both signaling outputs. All these results unravel a central role of mitochondria as sensors of proteotoxic stress and major contributors to JNK activation in CIN-induced aneuploid cells. Other sources of JNK activation might exist in aneuploid cells, including the reported impact of ROS in causing DNA damage and p53 activation in mammalian aneuploids (Li et al., 2010), which in flies results in the activation of JNK (McEwen and Peifer, 2005). Reducing the levels of autophagy or the activity of those pathways mediating autophagy induction increased the levels of JNK in CIN tissues, reinforcing the causal relationship between autophagy saturation, mitochondrial dysfunction and JNK activity (Figure S7F).

Aneuploidy-induced senescence, proteostasis and compensatory proliferation

CIN drives cellular senescence in mammalian cells as a consequence of the generation of highly aneuploid karyotypes (Barroso- Vilares et al., 2020; Macedo et al., 2018; Santaguida et al., 2017), and cellular senescence and its associated SASP can contribute to tissue repair, inflammation and tumorigenesis (Gorgoulis et al., 2019). We demonstrate that highly aneuploid fly epithelial cells enter a senescent state characterized by cell cycle arrest and a highly secretory phenotype, and that senescence contributes to compensatory proliferation and proteostasis. In contrast to mammalian cells, cell cycle arrest in fly epithelial cells is independent of the fly orthologues of p53 (Dp53) and p21/p27 (Dacapo), occurs in G2, and it is a result of JNK activation. The cell cycle arrest in G2 is a common response of *Drosophila* epithelial cells to various stresses, including DNA damage, polyploidy or tissue injury (Cosolo et al., 2019; Gerlach et al., 2018), and it is most probably due to the minor role played by Dp53 in mediating stress-driven cell cycle arrest in G1 (Ollmann et al., 2000). Interestingly, all other aspects of aneuploidy-induced senescence, including changes in cellular and nuclear size, and enlargement of the lysosomal compartment and the SASP, also rely on JNK activity (Figure 6, Figure S6). We also present evidence that JNK-driven senescence contributes, through the SASP, to proteostasis and tissue repair. Whereas IL-6-like Unpaired cytokines emanating from senescent cells contribute to the induction of autophagy, JNK, most probably through the production of the mitogenic molecule Wnt [Wingless in *Drosophila*, (Dekanty et al., 2012)], contributes to tissue repair. Maintenance of highly aneuploid cells in the tissue by apoptosis inhibition drives CIN-induced tumorigenesis most likely due to the chronic activation of the SASP (Dekanty et al., 2012).

Limitations of the study

By using a variety of genetic tools and characterizing the cellular behaviors observed in an epithelial tissue subjected to CIN, this work has elucidated the mechanisms by which aneuploidy-induced proteotoxic stress leads to the accumulation of dysfunctional mitochondria, which activate JNK in order to drive cellular senescence and orchestrate tissue homeostasis. Future studies will be needed to further characterize the molecular mechanisms used by mitochondria to act as sensing and signaling organelles in aneuploid cells and to identify the secreted molecular players that mediate all aspects of senescence-driven cell and tissue homeostasis.

Acknowledgements

We thank E.H. Baehrecke, P. Fernández-Fúnez, H. Herranz, G. Juhász, C. Lehner, N. Perrimon, F. Pignoni, T.E. Rusten, S. Luschnig, M. Miura, A. Teleman, A. J. Whitworth, A. Zorzano, the Bloomington *Drosophila* Stock Center (USA), the Vienna Drosophila Resource Center (Austria), and the Developmental Studies Hybridoma Bank (USA) for flies and antibodies, S. Ivanova, A. Zorzano and J. Colombelli for discussion, IRB Advanced Digital Microscopy, IRB Biostatistics/Bioinformatics and CCiTUB Cryon Microscopy facilities for technical support, and M. Muzzopappa for comments on the manuscript. This work was funded by *BFU2016-77587-P* and *PID2019-110082GB-I00* grants from the Spanish Ministry of Science and Innovation (Government of Spain), and ERDF "Una manera de hacer Europa". We gratefully acknowledge institutional funding from the Spanish Ministry of Science and Innovation through the Centres of Excellence Severo Ochoa Award, and from the CERCA Programme of the Catalan Government.

Author Contributions

All authors conceived and designed the experiments and analyzed the data. J.J., L.B., C.S.T., D.R. N.N.C. and M.C. performed the experiments. M.M. wrote the paper.

Declaration of interests

The authors declare no competing interests.

Figure legends

Figure 1. The ubiquitin-proteasome system is functioning near saturation in CIN tissues

(**A, B, D-J**) Wing discs of larvae expressing the indicated transgenes under the control of *en-gal4* (expressed in posterior, P, cells) and stained for MMP1-GFP (**A-B'**), Ref(2)P (red or white, **D**, **E**, **E'**), Ubiquitin (Ubq, green or white in **D**, **E**, **E'**, red in **J**), Htt-25Q (green, **F-G'),** CL1-GFP (green, **H-J**), and DAPI (blue or white). (**C**) Cartoon depicting the cellular response of an epithelium to Chromosomal Instability (CIN), where highly aneuploid cells delaminate to the basal (bs) side of the epithelium. (**K**) Adult eyes expressing the indicated transgenes under the control of *ey-gal4*. Higher magnifications of **A**, **B**, **E**, **G, I** (marked with white squares in **E**) are shown in **A'**, **B'**, **E'**, **G'**, **I'** and cross-sections of **A'** and **B'** are shown below. In all figures, the anterior-posterior (AP) boundary is depicted by a white line, delaminating cells by a cyan line and wing disc contours by a dotted line. Scale bars, 50 μm. See also Figure S1.

Figure 2. Autophagy plays a critical role in CIN tissues

(**A-E, G-J**) Wing discs of larvae expressing the indicated transgenes under the control of *en-gal4* and stained for Cherry-Atg8a (ChAtg8a, red or white, **A-E, G-G''**), Ref(2)P (green or white, **D-E'**, red, **H-I'**), Ubiquitin (Ubq, green or white, **H**, **H'**), CL1-GFP (green, **J, J'**), and DAPI (blue or white, **C**, **E**, **G**, **I- J'**). (**F**) Adult eyes expressing the indicated transgenes under the control of *ey-gal4*. (**K**) Scatter plots showing the amount of ChAtg8, Ref(2)P, Ubq and CL1-GFP signal per area of wing discs expressing the indicated transgenes. Mean and SD are shown. Student's t-test: *** $p<0.001$. Higher magnifications of **C**, **E**, **G**, **H**, **I**, **J** (marked with white squares in **C**, **E**, **G**, **I**) are shown in **C'**, **E'**, **G'**, **H'**, **I'**, **J'**. White arrowheads in **I** show Ref(2)P-positive signal in epithelial cells. Scale bars, 50 μm. See also Figure S2.

Figure 3. Autophagic flux is functioning near saturation in CIN tissues

(**A-C'**, **E-L**, **N**) Wing discs of larvae expressing the indicated transgenes under the control of *en-gal4* (**A-C', E-L**) or *ap-gal4* (**N**) and stained for Atg8a tagged with GFP (green) and mCherry (red, **A-C'**), Mitf 2.2-GFP (green or white, **E**, **F**), 4Mbox-GFP (green or white, **G**, **H**), Lysotracker (red or white, **I**, **J**), Lamp-GFP (green or white, **K**, **L**), Dcp1 (green or white, **N**), MyrT (red, **N**) and DAPI (white in **A-C**; blue or white in **F**, **H**, **J**, **L**, **N**). Higher magnifications of **A-C** are shown in **A'-C'**. (**D**, **N**) Histograms (**D**) and scatter plot (**N**) showing the percentage of red and yellow dots in GFP-mCherry-Atg8a-expressing wing discs (**D**) and Dcp1 signal per area (**N**) of wing discs expressing the indicated transgenes. Mean values and SD are shown. Chi-square test for

equality of proportion (**D**) and Student's t-test (**N**): *** p<0.001. (**M**) Adult eyes expressing the indicated transgenes under the control of *ey-gal4*. Scale bars, 50 μm. See also Figure S3.

Figure 4. UPR and HIF activation and TOR inhibition contribute to autophagy induction

(**A-F'**, **H-M'**, **O**) Wing discs of larvae expressing the indicated transgenes under the control of *en-gal4* (**A-F'**, **H-M'**) or *ap-gal4* (**O**) and stained for LDH-GFP, SIMA-GFP and ODD-GFP (green, **A-B'**), unk-GFP (green, **C-D'**), P-elf2a and Xbp1-GFP (green, **E-F'**), Cherry-Atg8a (ChAtg8a, red, **H-M'**), Dcp1 (green or white, **O**), MyrT(red, **O**) and DAPI (blue or white, **B'**, **D'**, **F'**, **H-M**, **O**). Higher magnifications of **B**, **D**, **F**, **H-M** (marked with white squares in **H-M**) are shown in **B'**, **D'**, **F'**, **H'-M'**. (**G**) Adult eyes expressing the indicated transgenes under the control of *ey-gal4*. (**N**, **O**) Scatter plots showing the amount of ChAtg8a (**N**) or Dcp1 (**O**) signal per area of wing discs expressing the indicated transgenes. Mean values and SD are shown. Dunnett's test: *** p<0.001. Scale bars, 50 μm. See also Figure S4.

Figure 5. Mitochondrial dysfunction as a source of ROS in CIN tissues

(**A-B'''**, **E-N'**,**R-W**) Wing discs of larvae expressing the indicated transgenes under the control of *en-gal4* (**A-B'''**, **E-N'**, **S-W**) or *ap-gal4* (**R**) and stained for MitoGFP (green or white, **A-B''', G-H'**), MitoTimer (green and red, **E-F''**), Ref(2)P (red, **G**), ChAtg8a (**H, H'**), MitoQC (green and red, **I-N'**), Dcp1 (green or white, **R**), MyrT (red, **R**), DHE (red or white, **S**), GstD-GFP (green, **T**, **V**), Mitosox (red or white, **U, W**), MMP1-GFP (green, **S, U**), and DAPI (blue or white). (**C**, **O**) TEM (**C**) and CLEM (**O**) of wing disc cells. Mitochondria are marked in green in **C** or labeled by the expression of MitoQC (red or yellow) in **O**. Higher magnifications of **A', B', E, F, H, I, J, M, N, O** (marked with white squares in **A', B', H, M, N O**) are shown in **A''-A''', B''- B''', E'- E'', F'- F'', I'- I'', J'-O**. (**D**, **P**, **R**, **V**, **W**) Histograms (**D**, **P**) and scatter plots (**R**, **V**, **W**) showing mitochondria density and length (**D**), the number of MitoQC-positive dots per wing disc and the percentage of red and yellow dots (**P**), and the amount of Dcp1 (**R**), GstD-GFP (**V**) or Mitosox (**V**) signal per area in wing discs expressing the indicated transgenes. Mean values and SD are shown. Chi-square test for equality of proportions (**P**), Student's t-test (**D**, **R**) or Dunnett's test (**V**, **W**): *** p<0.001. (**Q**) Adult eyes expressing the indicated transgenes under the control of *ey-gal4*. Arrows point to Ref(2)P-positive signal colocalizing with MitoGFP in **G**, to large ChAtg8a aggregates colocalizing with MitoGFP in **H**, and to mitolysosomes in **I'', K, L, O**. Arrowheads and asterisks in **K-O** point to yellow MitoQC-positive puncta and yellow MitoQC-positive aggregates, respectively. See also Figure S5 and Videos S1-S6.

Figure 6. A role of JNK in CIN-induced senescence

(**A, C, D, E, G**) Wing discs of larvae expressing the indicated transgenes under the control of *en-gal4* and stained for MMP1 (red, **A**, **C**), pH3 (green or white, **A**), EdU (green or white, **C**), FlyFucci (ub-GFP-E2F1$_{1-230}$ and ub-mRFP1-NLS-CycB$_{1-266}$) to label cells in G1 (green), G2 (yellow) and S (red) phases (**D**), MMP1-GFP (red, **E**), MyrT (green, **E**), senescence-associated (SA) β-galactosidase (green or white, **G**) and DAPI (blue or white, **A**, **C**, **E**, **G**). High magnification of the squared regions is shown in **A**, **C**, **D**, **G**. (**B**, **F**) Scatter plots showing mitotic activity (**B**) and nuclear size (**F**) of delaminated cells of the indicated genotypes. Mean and SD are shown. Student's t-test (**B**) or Tukey's test (**F**): *** p<0.001. Scale bars, 50 μm (**A**, **C**, **D**, **G**), 10 μm (in high magnifications in **D**), 5 μm (**E**). See also Figure S6.

Figure 7. CIN-induced senescence contributes to tissue repair and proteostasis

(**A**) Adult eyes expressing the indicated transgenes under the control of *ey-gal4*. (**B**, **D**-**G**) Wing discs of larvae expressing the indicated transgenes under the control of *en-gal4* and stained for pH3 (green or white, **B**), Ci (red, **B**), Cherry-Atg8a (ChAtg8a, red, **D**), lysotracker (red, **E**), Ref(2)P (red, **F**), CL1-GFP (green, **G**). Bottom panels in **D**-**E** are higher magnifications of the regions marked with a white square in the wing discs shown in upper panels. Scale bars, 50 μm . (**C**, **D'**, **E'**, **F'**, **G'**). Scatter plots showing mitotic activity and P/A ratio (**C**), Cherry-Atg8a (**D'**), lysotracker (**E'**) and CL1-GFP (**F'**) signal per area in wing disc of the indicated genotypes. Mean and SD are shown. Tukey's (**C**), Dunnett's (**D'**) or Student's t-test (**E'**-**G'**): ** p<0.01, *** p<0.001. (**H**) Cartoon depicting the pathway that leads to aneuploidy-induced senescence. See also Figure S7.

STAR methods

Resource availability

Lead Contact

Further information and requests for resources and reagents should be directed to and will be fulfilled by the Lead Contact, Marco Milán (marco.milan@irbbarcelona.org).

Materials Availability

Strains generated in the course of this work are freely available to academic researchers through the Lead Contact.

Data and Code Availability

This study did not generate datasets or codes.

Experimental Model and Subject Details

Fly maintenance, husbandry and transgene expression

Strains of *Drosophila melanogaster* were maintained on standard medium (4% glucose, 55 g/L yeast, 0.65% agar, 28 g/L wheat flour, 4 ml/L propionic acid and 1.1 g/L nipagin) at 25°C in light/dark cycles of 12 hours. Sex of experimental larvae was not considered relevant to this study and was not determined. The strains used in this study are summarized in the Key Resources Table.

Standard induction of CIN

Females of the following genotype: *en-gal4, UAS-p35/CyO,GFP; UAS-rod-RNAi/TM6B, tub-Gal80* were crossed with males carrying the corresponding transgenes and allowed to lay eggs on standard fly food for 24 h at 25°C. Larvae were kept at 29°C for 5 days before dissection. Experimental flies and control individuals were grown in parallel.

Cell death experiments

Flies were allowed to lay eggs on standard fly food for 24 h at 25°C and kept at 25°C for another 24 h. Larvae were then switched to 29ºC and maintained for 3 days before dissection. Experimental flies and control individuals were grown in parallel.

CIN eye model experiments

Adult eye experiments: females carrying either the *ey-gal4* driver alone (control) or the *ey-gal4* driver together with the *UAS-bub3-RNAi* transgene (CIN) were crossed with males of the indicated genotypes and allowed to lay eggs on standard fly food for 24 h at 25°C. Progeny was kept at 25°C until they eclosed. Experimental flies and control individuals were grown in parallel. The eye phenotype was monitored in adult males. Information about the transgenes (name and origin) used, the figure where they appear, the total number (n) of eyes scored and the frequency (in %) of the different phenotypes observed (wild-type, mild and strong phenotype) is included in Table S1.

Eye disc experiments: Flies were allowed to lay eggs on standard fly food for 24 h at 25°C and kept at 25°C for another 24 h. Larvae were then switched to 29ºC and maintained for 3 days before dissection. Experimental flies and control individuals were grown in parallel. Divergent from wing imaginal discs, eye discs were observed with pyknotic nuclei even in the presence of *p35* overexpression, suggesting its loss over time.

Method Details

Immunohistochemistry

Wing imaginal discs of third instar larvae were dissected in cold PBS, fixed in 4% formaldehyde for 20 min, rinsed three times in PBT (PBS1%, 0.2% Triton), blocked for 1 h in BBT (PBS1X, 0.3% BSA, 0.2% Triton, 250 mM NaCl) and incubated overnight with the following antibodies: mouse anti-MMP1 (1:20) (14A3D2, Developmental Studies Hybridoma Bank, DSHB); rabbit anti-PH3 (1:1000; Merk Millipore); rat anti-Ci (1:10; 2A1, DSHB); rabbit anti-cleaved Dcp1 (1:100; 9578 S, Cell Signaling Technology); rabbit anti-Ref(2)P (1:5000, Tor Erik); mouse anti-Ubiquitin (1:100, Enzo Life Science); mouse anti-P-H2Av (1:500, 2618077, DSHB). Discs were rinsed with PBT and incubated with secondary antibodies [Cy2, Cy3, Cy5 and Alexa 647 (1:400), Jackson ImmunoResearch] and DAPI for 2 h. After 3 PBT washes, discs were kept on mounting media (80 ml glycerol + 10 ml PBS 10x + 0.8 ml N-propyl-gallate 50%).

Leica SP5, Zeiss LSM780 and Zeiss LSM880 (with airyscan plus super resolution) confocal microscopes were used. The most representative image is shown in all experiments. At least 10-15 wing discs per genotype were imaged.

DNA synthesis

Click-iT™ Plus EdU Alexa Fluor™ 647 Imaging Kit from Invitrogen (C10640) was used to measure DNA synthesis (S phase) in proliferating cells, following the manufacturer's indications. EdU (5-ethynyl-2´-

deoxyuridine) provided in the kit is a nucleoside analogue of thymidine and is incorporated into DNA during active DNA synthesis. Time of incubation with EdU: 15 min.

SA-β-galactosidase assay

CellEvent™ senescence green detection kit from Invitrogen (C10850) was used to detect senescence-associated β-galactosidase (SA-β-gal) activity, following the manufacturer's instructions. Wing discs were fixed with 4% PFA, washed (1% BSA in PBS) and then incubated in working solution for 2 h at 37ºC. Discs were then washed in PBS and mounted for confocal imaging.

Fluorescent-based ROS detection assays

Dihydroethidium (DHE): For the detection of Superoxide radicals, imaginal discs were dissected in Schneider's medium followed by incubation in 0.3mM DHE (Molecular Probes, Cat# D11347) in Schneider's medium for 5 min at RT in the dark. After washing the tissues with PBS1X buffer (pH7.2), they were briefly fixed in 8% paraformaldehyde for 10 min at RT and incubated for 10 min with DAPI in PBT. Tissues were imaged in a Zeiss LSM780 confocal microscope.

Mitosox: For the detection of Superoxide radicals, imaginal discs were dissected in Schneider's medium at RT, and then incubated in 5 μM MitoSOX™ redDHE (Molecular Probes, Cat# M36008) in Schneider's medium for 10 min at 37°C, protected from light. After washing the tissues with warm Schneider's medium, the discs were mounted in Schneider's medium and live-imaged immediately in a Zeiss LSM780 confocal microscope. The MMP1-GFP reporter was used to identify the delaminating cell population in the sample.

Tetramethylrhodamine Ethyl Ester (TMRE) assay

Fluorescent dye was used to measure mitochondrial membrane potential (high fluorescence, hyperpolarized, low fluorescence, depolarized). Wing discs were dissected in Schneider's medium followed by incubation in 0.1μM TMRE (Invitrogen, #T669) in Schneider's medium for 10 min at RT in the dark. After washing the tissues with Schneider's medium twice, they were mounted in Schneider's medium and immediately imaged. The MMP1-GFP reporter was used to identify the delaminating cell population in the sample.

Flow Cytometry analysis

Wing discs of larvae of the following genotypes (1) *ap-gal4,UAS-MyrT;UAS-p35 (2) ap-gal4,UAS-rod-RNAi,UAS-MyrT/MMP1-GFP; UAS-p35* and (2) *ap-gal4,mud-RNAi,UAS-MyrT/MMP1-GFP; UAS-p35* (3) *ey-gal4;UAS-p35* (4) *ey-gal4,UAS-bub3-i;UAS-p35* were dissected in cold PBS, dissociated with Trypsin-EDTA,

fixed with formaldehyde 4% for 20 min and permeabilized in ethanol 70% for 2 hours. Fixed cells were stained with DAPI. Cells from the ventral compartment (MyrT-negative, MMP1-GFP-negative), dorsal compartment (MyrT-positive, MMP1-GFP-negative) and delaminating cell population (MyrT-positive, MMP1-GFP-positive) were sorted by FACS. Delaminated cells activate JNK and drive *MMP1-GFP* expression. Then, GFP positive cells represent the delaminated cell population. For eye disc experiments, cells were not sorted based on JNK expression. Instead, all cells were accounted. DAPI fluorescence was determined by flow cytometry using a MoFlo flow cytometer (DakoCytomation, Fort Collins, CO). Excitation of the sample was carried out using a Coherent Enterprise II argon-ion laser. Excitation with the UV laser (440 nm) permits the acquisition of forward-scatter (FS), side-scatter (SS) and DNA content, the blue laser (530 nm) fluorescence from GFP and the green laser (610 nm) fluorescence from Tomato. Doublets were discriminated using an integral/peak dotplot of DAPI fluorescence. Optical alignment was based on optimized signal from 10 µm fluorescent beads (Flowcheck, Coulter Corporation, Miami, FL). DNA analysis (Ploidy analysis) on single fluorescence histograms was done using Multicycle software (Phoenix Flow Systems, San Diego, CA).

Comet assay

The Comet Assay Kit (Trevigen, Catalog #4250-050K) was performed as described in (Rimkus and Wassarman, 2018) to detect Double Strand Breaks (DSBs) in DNA at a single-cell level, with the following modifications. Briefly, 6 wing imaginal discs were dissected and placed in 1,5 ml Eppendorf tube with 100 µl of cold PBS. Samples were homogenized with plastic pestles for 3 sec, and 10 µl of homogenate was added to 100 µl of LMA-agarose that had been boiled and cooled to 37ºC in a heat block. Comets were imaged using an ECLIPSE E800 + OLYMPUS DP72 upright microscope with a 10X objective. For each sample, >100 comets were imaged and analyzed using CaspLab Software. Damage was quantified as the comet tail moment, which is defined as the product of the tail length and the fraction of total DNA in the tail (Tail moment=tail length x % of DNA in the tail). Unpaired equal-variance two-tail t-test was performed using GraphPad Prism 7 Project to compare comet tail moment between pairs of samples.

Confocal microscopy.

Samples were analyzed using the following confocal microscopes: Leica SP5, LSM 780 Zeiss and LSM880 Zeiss fitted with a Fast Airyscan module (Carl Zeiss). Z-stacks were acquired using either the laser scanning confocal mode or the High Resolution mode (Airyscan). Image acquisition was done with either 100x, 63x, 40x

or 25x oil lenses. Airyscan raw images were reconstructed with the default 3D Airyscan algorithm of ZEN black software from Zeiss in Figure 5 (panels A´´´, B´´´, E´´, F´´, L, M), Figure S3 (panel F), Figure S5 (panels A, B, B´, C, D, D´, H, I, J, K, L), Figure S6 (panels B, C), and Videos S1, S2, S4, S5.

Structured Illumination microscopy (SIM)

SIM data shown in Figure 5 (panels H and N) and Videos S3 and S6 were acquired on a LSM 880 Zeiss confocal microscope equipped with an Elyra PS1 module and a piezo stage. Image acquisition was done with either 100x or 63x oil lenses. Grid rotations were restricted to three to avoid bleaching. SIM images were reconstructed with the ZEN black software from Zeiss and with the use of Max Isotropic and the Baseline Shifted algorithms.

3D reconstructions

3D reconstructions in Videos S1-S6 were done with the use of Imaris 9.0.1 and intensity-based surfaces were created after background subtraction.

Correlative light electron microscopy (CLEM)

A previously published protocol for eye imaginal discs (Katheder et al., 2017) was followed for preparation of wing imaginal discs. Serial sections (~100nm) of wing imaginal discs were cut on an Ultracut UCT ultramicrotome (Leica) and collected on 200µm-mesh carbon-coated grids. Water was added and grids were imaged with the use of tile scanning multichannel confocal imaging with Z-stacks (LSM 880, 63x oil lens, with oversampling). The same areas were imaged with the use of TEM (80kV in a JEOL-JEM 1010 electron microscope). Confocal images were flipped horizontally and rotated 90^{o} degrees for overlaying. ImageJ (Rueden et al., 2017) was used to subtract background and filter the fluorescence images. Fluorescence and electron microscopy images were rescaled and registered with the use of ec-CLEM, an ICY imaging software plugin (Paul-Gilloteaux et al., 2017). At least 15 landmarks were taken per image and the default rigid registration algorithm was used.

Expansion microscopy

Protocol was adopted from (Tillberg et al., 2016) and modified. Tissues (after normal fixation and antibody staining) were treated with 0.1 mg/ml Acryloyl X (Life Technologies) in PBS at room temperature, overnight. Cells were then washed in monomer solution (1x PBS, 2 M NaCl, 2.5% acrylamide, 0.15% Methylenbisacrylamide, 8.625% sodium acrylate) and embedded in monomer solution containing 0.2% APS

and 0.2% TEMED. Gels were polymerized for 2 h at 37°C and then digested with 8 U/ml Proteinase K for 4 h at 37°C. Gels were expanded in MilliQ (expansion factor ~5) and mounted on poly-L-lysine-coated coverslips and imaged by Airyscan in Figure 5M and Figure S5H.

Quantification and Statistical Analysis

Tissue growth (P/A ratio)

The sizes of the whole wing disc (based on DAPI staining) and the anterior (A) and posterior (P) compartments (based on Ci expression) were measured manually using Fiji Software (NIH, USA) on apical sections (epithelium) of the wing disc obtained using a Zeiss LSM780 confocal microscope at 25X glycerol immersion objective. The ratio between the posterior and anterior (PA) compartment sizes was calculated.

Ref(2)P, Ubq, MMP1, Mitosox and Dcp1

The sizes of the posterior (for Ref(2)P, Ubq and MMP1) or the dorsal compartments (for Dcp1) based on Ci and MyrT expression respectively, or the wing pouch and hinge area (for Mitosox) were measured (polygonal tool) using Fiji Software (NIH, USA), while the Ref(2)P/Ubq/Dcp1/Mitosox signal was measured upon setting a fluorescence threshold for the corresponding channel. Image stacks were obtained using a Zeiss LSM780 confocal microscope at 25X oil immersion objective with 2 μm per optical section to cover the entire thickness of each disc. Maximum intensity Z-projection was performed on the stacks prior to quantification. The ratio between the Ref(2)P/Ubq/Dcp1-positive area and the corresponding compartment (posterior or dorsal) was calculated. All genotypes included in each plot were analyzed in parallel. And, in the case of Dcp1 signal and Mitosox, scatter plots represent fold-change induction according to their respective control.

Mitotic activity (pH3)

Quantification of mitosis in delaminating cells (based on MMP1 expression and DAPI morphology, Figure 6B) or in the wing pouch and hinge region (Figure 7C) was performed by counting mitotic cells (pH3 positive cells) using the Fiji Software (NIH, USA). Image stacks were obtained using a Zeiss LSM780 confocal microscope at 40X glycerol immersion objective with 2 μm per optical section to cover the entire thickness of each disc. The ratio between number of mitotic cells and the MMP1-positive area (Figure 6B) or the ratio between the amount of pH3 cells in the posterior versus the anterior region (Figure 7C) was calculated.

ChAtg8a and lysotracker (LTR)

Fiji Software (NIH, USA) was used to measure the MMP1-positive region (polygonal tool) and the ChAtg8a/LTR-positive area upon setting a fluorescence threshold for the red channel in single plane sections of the delaminating cells (positive for MMP1). Image stacks were obtained using a Zeiss LSM780 confocal microscope, 40X oil immersion objective with 2 µm per optical section to cover the entire thickness of each disc. Several optical sections of a minimum of 6 different wing discs were scored and the ratio between the ChAtg8a-positive area and the posterior compartment was calculated.

GFP-Ch-Atg8a and MitoQC

Fiji Software (NIH, USA) was used to manually measure the MMP1-positive region (polygonal tool) and to manually count the number of big and small yellow dots, and big and small red dots in this region of the dual reporters GFP-mCherry-Atg8 (Figure 3D) and MitoQC (Figure 5I). Image stacks were obtained using a Zeiss LSM780 confocal microscope, 40X oil immersion objective with 2 µm per optical section to cover the entire thickness of each disc. Several optical sections of a minimum of 6 different wing discs were scored and the ratio between number of dots per MMP1 area or the frequencies of the dots (in percentage).

Fly-Fucci quantification

Image stacks were obtained using a Zeiss LSM780 confocal microscope at 63X oil immersion objective with 1 µm per optical section to cover the entire thickness of the delaminating population of cells (CIN-tissues) or a region of interest within the asynchronously dividing cells of the epithelium, thereby avoiding the zone of non-proliferating cell (control wing disc) under identical confocal settings. The number of red, green or red and green cells were counted manually and percentages were calculated.

Mitochondria density and length

Mitochondria density: three whole wing discs of control and CIN tissues expressing Mito-GFP under the control of the *en-gal4* driver were selected, images were taken at 100X with tile scan and stitching at super-resolution quality using Airyscan. Mitochondria accumulation (%) was calculated from each sample and t-test was conducted based on average values.

Mitochondrial length: the wing pouch region of control and CIN tissues expressing Mito-GFP under the control of the *en-gal4* driver was selected and small 3D stacks (1.5-2 microns thick, roughly a cell thickness) were projected with SUM projection. Fiji Software (NIH, USA) was used to apply manual threshold and watershed algorithm to segment the images and measure particles (mitochondria) length. A minimum number of

25000 particles in total were measured. Average length in microns was calculated from each image (five per genotype) and t-test was conducted based on average values.

Mito-GFP-Ref(2)P colocalization quantification

The Just Another Colocalization Plugin (JACoP) plugin from Fiji Software (NIH, USA) was used to quantify the grade of overlap of Mito-GFP aggregates and Ref(2)P fluorescent signals in images with stacks (CIN-tissues). The overlap coefficient is calculated as the Pearson's coefficient with the mean intensity value of both channels being taken out of the expression. Average value of overlapping coefficient after applying manual threshold was 0.74 (number of wing discs=9).

Statistical analysis

Statistical analysis was performed by unpaired equal-variance two-tail Student's t-test when comparing the difference in means of a single experimental group with a control, or by a chi-square test for equality of proportion of a single experimental group with a control. Differences were considered significant when p values were less than 0.001 (***), 0.01 (**), or 0.05 (*). All genotypes included in each histogram or scatter plot were subjected to the same experimental conditions (temperature and time of transgene induction) and analyzed in parallel. Mean values and standard deviations were calculated and the corresponding statistical analysis and graphical representations were carried out with GraphPad Prism 7.0 statistical software. ANOVA followed by Dunnett's test was applied when comparing multiple experimental groups with a common control. ANOVA followed by Tukey's test was used for comparing the equality of means in all possible group pairs. Differences were considered significant when adjusted p values were less than 0.001 (***), 0.01 (**), or 0.05 (*). All tests were performed after log-transformation of the data. However, for clarity of representation, data are shown in the original scale. Statistical analysis was carried out with the multcomp R package (Hothorn et al., 2008). Information about the n values, p values, and statistical tests used can be found in the figure legends and in Table S2.

Supplementary Movies

Video S1. Filamentous array of mitochondria in a wild type wing disc, related to Figure 5.

3D reconstruction of a wing disc expressing p35 and Mito-GFP (green) under the control of the *en-gal4* driver.

Video S2. **Fragmented mitochondria in a wing disc subjected to CIN, related to Figure 5.**

3D reconstruction of a wing disc expressing rod-RNAi, p35 and Mito-GFP (green) under the control of the *en-gal4* driver.

Video S3. Co-localization of large autophagic cargos and mitochondria in CIN-induced aneuploid cells, related to Figure 5.

3D reconstruction of a wing disc, and rod-RNAi, p35 and Mito-GFP (green) under the control of the *en-gal4* driver and ChAtg8a (red) under the control of the Atg8a promoter.

Video S4. Large autophagic cargo with fragmented mitochondria in a CIN-induced aneuploid cell, related to Figure 5.

3D reconstruction of a wing disc expressing rod-RNAi, p35 and Mito-GFP (green) under the control of the *en-gal4* driver and ChAtg8a (red) under the control of the Atg8a promoter.

Video S5. **Mitophagy induction and saturation in a wing disc subjected to CIN, related to Figure 5.**

3D reconstruction of a wing disc expressing rod-RNAi, p35 and Mito-QC (red and green) under the control of the *en-gal4* driver.

Video S6. **Mitophagy saturation in CIN-induced aneuploid cells, related to Figure 5.**

3D reconstruction of a wing disc expressing rod-RNAi, p35 and Mito-QC (red and green) under the control of the *en-gal4* driver.

References

Aparicio, R., Rana, A., and Walker, D.W. (2019). Upregulation of the Autophagy Adaptor p62/SQSTM1 Prolongs Health and Lifespan in Middle-Aged Drosophila. Cell Rep. *28*, 1029-1040.e5.

Bakhoum, S.F., Ngo, B., Laughney, A.M., Cavallo, J.-A., Murphy, C.J., Ly, P., Shah, P., Sriram, R.K., Watkins, T.B.K., Taunk, N.K., et al. (2018). Chromosomal instability drives metastasis through a cytosolic DNA response. Nature *553*, 467–472.

Barroso- Vilares, M., Macedo, J.C., Reis, M., Warren, J.D., Compton, D., and Logarinho, E. (2020). Small-molecule inhibition of aging- associated chromosomal instability delays cellular senescence. EMBO Rep. *21*, e49248.

Ben-David, U., and Amon, A. (2020). Context is everything: aneuploidy in cancer. Nat. Rev. Genet. *21*, 44–62.

Benhra, N., Barrio, L., Muzzopappa, M., and Milán, M. (2018). Chromosomal Instability Induces Cellular Invasion in Epithelial Tissues. Dev. Cell *47*, 161-174.e4.

Borch Jensen, M., Qi, Y., Riley, R., Rabkina, L., and Jasper, H. (2017). PGAM5 promotes lasting FoxO activation after developmental mitochondrial stress and extends lifespan in Drosophila. Elife *6*.

Bouché, V., Espinosa, A.P., Leone, L., Sardiello, M., Ballabio, A., and Botas, J. (2016). Drosophila Mitf regulates the V-ATPase and the lysosomal-autophagic pathway. Autophagy *12*, 484–498.

Chakraborty, J., Stockum, S., Marchesan, E., Caicci, F., Ferrari, V., Rakovic, A., Klein, C., Antonini, A., Bubacco, L., and Ziviani, E. (2018). USP 14 inhibition corrects an in vivo model of impaired mitophagy. EMBO Mol. Med. *10*.

Chandel, N.S. (2014). Mitochondria as signaling organelles. BMC Biol. *12*, 34.

Clemente-Ruiz, M., Muzzopappa, M., and Milán, M. (2014). Tumor suppressor roles of CENP-E and Nsl1 in Drosophila epithelial tissues. Cell Cycle *13*, 1450–1455.

Clemente-Ruiz, M., Murillo-Maldonado, J.M., Benhra, N., Barrio, L., Pérez, L., Quiroga, G., Nebreda, A.R., and Milán, M. (2016). Gene Dosage Imbalance Contributes to Chromosomal Instability-Induced Tumorigenesis. Dev. Cell *36*, 290–302.

Cosolo, A., Jaiswal, J., Csordás, G., Grass, I., Uhlirova, M., and Classen, A.-K. (2019). JNK-dependent cell cycle stalling in G2 promotes survival and senescence-like phenotypes in tissue stress. Elife *8*.

Dekanty, A., Barrio, L., Muzzopappa, M., Auer, H., and Milan, M. (2012). Aneuploidy-induced delaminating

cells drive tumorigenesis in Drosophila epithelia. Proc. Natl. Acad. Sci. *109*, 20549–20554.

Gerlach, S.U., Eichenlaub, T., and Herranz, H. (2018). Yorkie and JNK Control Tumorigenesis in Drosophila Cells with Cytokinesis Failure. Cell Rep. *23*, 1491–1503.

Gething, M.-J. (1999). Role and regulation of the ER chaperone BiP. Semin. Cell Dev. Biol. *10*, 465–472.

Gorgoulis, V., Adams, P.D., Alimonti, A., Bennett, D.C., Bischof, O., Bishop, C., Campisi, J., Collado, M., Evangelou, K., Ferbeyre, G., et al. (2019). Cellular Senescence: Defining a Path Forward. Cell *179*, 813–827.

Hanna, J., Hathaway, N.A., Tone, Y., Crosas, B., Elsasser, S., Kirkpatrick, D.S., Leggett, D.S., Gygi, S.P., King, R.W., and Finley, D. (2006). Deubiquitinating Enzyme Ubp6 Functions Noncatalytically to Delay Proteasomal Degradation. Cell *127*, 99–111.

Hay, B.A., Wolff, T., and Rubin, G.M. (1994). Expression of baculovirus P35 prevents cell death in Drosophila. Development *120*, 2121–2129.

Haynie, J.L., and Bryant, P.J. (1977). The effects of X-rays on the proliferation dynamics of cells in the imaginal wing discs of Drosophila melanogaster. Wilhelm Roux's Arch. *183*, 85–100.

He, C., and Klionsky, D.J. (2009). Regulation Mechanisms and Signaling Pathways of Autophagy. Annu. Rev. Genet. *43*, 67–93.

Hegedűs, K., Takáts, S., Boda, A., Jipa, A., Nagy, P., Varga, K., Kovács, A.L., and Juhász, G. (2016). The Ccz1-Mon1-Rab7 module and Rab5 control distinct steps of autophagy. Mol. Biol. Cell *27*, 3132–3142.

Hernandez-Segura, A., Nehme, J., and Demaria, M. (2018). Hallmarks of Cellular Senescence. Trends Cell Biol. *28*, 436–453.

Hothorn, T., Bretz, F., and Westfall, P. (2008). Simultaneous Inference in General Parametric Models. Biometrical J. *50*, 346–363.

Katheder, N.S., Khezri, R., O'Farrell, F., Schultz, S.W., Jain, A., Rahman, M.M., Schink, K.O., Theodossiou, T.A., Johansen, T., Juhasz, G., et al. (2017). Microenvironmental autophagy promotes tumour growth. Nature *541*, 417–420.

Laker, R.C., Xu, P., Ryall, K.A., Sujkowski, A., Kenwood, B.M., Chain, K.H., Zhang, M., Royal, M.A., Hoehn, K.L., Driscoll, M., et al. (2014). A Novel MitoTimer Reporter Gene for Mitochondrial Content, Structure, Stress, and Damage in Vivo. J. Biol. Chem. *289*, 12005–12015.

Lavista-Llanos, S., Centanin, L., Irisarri, M., Russo, D.M., Gleadle, J.M., Bocca, S.N., Muzzopappa, M., Ratcliffe, P.J., and Wappner, P. (2002). Control of the Hypoxic Response in Drosophila melanogaster by the Basic Helix-Loop-Helix PAS Protein Similar. Mol. Cell. Biol. *22*, 6842–6853.

Lee, J.J., Sanchez-Martinez, A., Zarate, A.M., Benincá, C., Mayor, U., Clague, M.J., and Whitworth, A.J. (2018). Basal mitophagy is widespread in Drosophila but minimally affected by loss of Pink1 or parkin. J. Cell Biol. *217*, 1613–1622.

Levine, M.S., Bakker, B., Boeckx, B., Moyett, J., Lu, J., Vitre, B., Spierings, D.C., Lansdorp, P.M., Cleveland, D.W., Lambrechts, D., et al. (2017). Centrosome Amplification Is Sufficient to Promote Spontaneous Tumorigenesis in Mammals. Dev Cell *40*, 313-322 e5.

Li, M., Fang, X., Baker, D.J., Guo, L., Gao, X., Wei, Z., Han, S., van Deursen, J.M., and Zhang, P. (2010). The ATM-p53 pathway suppresses aneuploidy-induced tumorigenesis. Proc. Natl. Acad. Sci. *107*, 14188–14193.

Lidsky, P. V., Lukyanov, K.A., Misra, T., Handke, B., Mishin, A.S., and Lehner, C.F. (2018). A genetically encoded fluorescent probe for imaging of oxygenation gradients in living Drosophila. Development *145*, dev156257.

Lőw, P., Varga, Á., Pircs, K., Nagy, P., Szatmári, Z., Sass, M., and Juhász, G. (2013). Impaired proteasomal degradation enhances autophagy via hypoxia signaling in Drosophila. BMC Cell Biol. *14*, 29.

Lucchesi, J.C., and Kuroda, M.I. (2015). Dosage Compensation in Drosophila. Cold Spring Harb. Perspect. Biol. *7*, a019398.

Macedo, J.C., Vaz, S., Bakker, B., Ribeiro, R., Bakker, P.L., Escandell, J.M., Ferreira, M.G., Medema, R., Foijer, F., and Logarinho, E. (2018). FoxM1 repression during human aging leads to mitotic decline and aneuploidy-driven full senescence. Nat. Commun. *9*, 2834.

Martin-Blanco, E., Gampel, A., Ring, J., Virdee, K., Kirov, N., Tolkovsky, A.M., and Martinez-Arias, A. (1998). puckered encodes a phosphatase that mediates a feedback loop regulating JNK activity during dorsal closure in Drosophila. Genes Dev *12*, 557–570.

McEwen, D.G., and Peifer, M. (2005). Puckered, a Drosophila MAPK phosphatase, ensures cell viability by antagonizing JNK-induced apoptosis. Development *132*, 3935–3946.

Milan, M., Campuzano, S., and Garcia-Bellido, A. (1996). Cell cycling and patterned cell proliferation in the

Drosophila wing during metamorphosis. Proc. Natl. Acad. Sci. *93*, 11687–11692.

Milán, M., Clemente-Ruiz, M., Dekanty, A., and Muzzopappa, M. (2014). Aneuploidy and tumorigenesis in Drosophila. Semin. Cell Dev. Biol. *28*, 110–115.

Misra, T., Baccino-Calace, M., Meyenhofer, F., Rodriguez-Crespo, D., Akarsu, H., Armenta-Calderón, R., Gorr, T.A., Frei, C., Cantera, R., Egger, B., et al. (2017). A genetically encoded biosensor for visualising hypoxia responses in vivo. Biol. Open *6*, 296–304.

Mokranjac, D. (2020). How to get to the other side of the mitochondrial inner membrane – the protein import motor. Biol. Chem. *401*, 723–736.

Morais da Silva, S., Moutinho-Santos, T., and Sunkel, C.E. (2013). A tumor suppressor role of the Bub3 spindle checkpoint protein after apoptosis inhibition. J Cell Biol *201*, 385–393.

Muzzopappa, M., Murcia, L., and Milán, M. (2017). Feedback amplification loop drives malignant growth in epithelial tissues. Proc. Natl. Acad. Sci. *114*, E7291–E7300.

Nakajima, Y., Meyer, E.J., Kroesen, A., McKinney, S.A., and Gibson, M.C. (2013). Epithelial junctions maintain tissue architecture by directing planar spindle orientation. Nature *500*, 359–362.

Nezis, I.P., Simonsen, A., Sagona, A.P., Finley, K., Gaumer, S., Contamine, D., Rusten, T.E., Stenmark, H., and Brech, A. (2008). Ref(2)P, the Drosophila melanogaster homologue of mammalian p62, is required for the formation of protein aggregates in adult brain. J. Cell Biol. *180*, 1065–1071.

Noda, T., and Ohsumi, Y. (1998). Tor, a Phosphatidylinositol Kinase Homologue, Controls Autophagy in Yeast. J. Biol. Chem. *273*, 3963–3966.

Ollmann, M., Young, L.M., Di Como, C.J., Karim, F., Belvin, M., Robertson, S., Whittaker, K., Demsky, M., Fisher, W.W., Buchman, a, et al. (2000). Drosophila p53 is a structural and functional homolog of the tumor suppressor p53. Cell *101*, 91–101.

Owusu-Ansah, E., Song, W., and Perrimon, N. (2013). Muscle Mitohormesis Promotes Longevity via Systemic Repression of Insulin Signaling. Cell *155*, 699–712.

Pandey, U.B., Nie, Z., Batlevi, Y., McCray, B.A., Ritson, G.P., Nedelsky, N.B., Schwartz, S.L., Diprospero, N.A., Knight, M.A., Schuldiner, O., et al. (2007). HDAC6 rescues neurodegeneration and provides an essential link between autophagy and the UPS. Nature *447*, 859–863.

Paul-Gilloteaux, P., Heiligenstein, X., Belle, M., Domart, M.-C., Larijani, B., Collinson, L., Raposo, G., and

Salamero, J. (2017). eC-CLEM: flexible multidimensional registration software for correlative microscopies. Nat. Methods *14*, 102–103.

Phinney, D.G., Di Giuseppe, M., Njah, J., Sala, E., Shiva, S., St Croix, C.M., Stolz, D.B., Watkins, S.C., Di, Y.P., Leikauf, G.D., et al. (2015). Mesenchymal stem cells use extracellular vesicles to outsource mitophagy and shuttle microRNAs. Nat. Commun. *6*, 8472.

de Poot, S.A.H., Tian, G., and Finley, D. (2017). Meddling with Fate: The Proteasomal Deubiquitinating Enzymes. J. Mol. Biol. *429*, 3525–3545.

Ramdzan, Y.M., Trubetskov, M.M., Ormsby, A.R., Newcombe, E.A., Sui, X., Tobin, M.J., Bongiovanni, M.N., Gras, S.L., Dewson, G., Miller, J.M.L., et al. (2017). Huntingtin Inclusions Trigger Cellular Quiescence, Deactivate Apoptosis, and Lead to Delayed Necrosis. Cell Rep. *19*, 919–927.

Rana, A., Rera, M., and Walker, D.W. (2013). Parkin overexpression during aging reduces proteotoxicity, alters mitochondrial dynamics, and extends lifespan. Proc. Natl. Acad. Sci. *110*, 8638–8643.

Rong, Y., McPhee, C.K., Deng, S., Huang, L., Chen, L., Liu, M., Tracy, K., Baehrecke, E.H., Yu, L., and Lenardo, M.J. (2011). Spinster is required for autophagic lysosome reformation and mTOR reactivation following starvation. Proc. Natl. Acad. Sci. *108*, 7826–7831.

Rowald, K., Mantovan, M., Passos, J., Buccitelli, C., Mardin, B.R., Korbel, J.O., Jechlinger, M., and Sotillo, R. (2016). Negative Selection and Chromosome Instability Induced by Mad2 Overexpression Delay Breast Cancer but Facilitate Oncogene-Independent Outgrowth. Cell Rep. *15*, 2679–2691.

Rueden, C.T., Schindelin, J., Hiner, M.C., DeZonia, B.E., Walter, A.E., Arena, E.T., and Eliceiri, K.W. (2017). ImageJ2: ImageJ for the next generation of scientific image data. BMC Bioinformatics *18*, 529.

Ryoo, H.D., Domingos, P.M., Kang, M.-J., and Steller, H. (2007). Unfolded protein response in a Drosophila model for retinal degeneration. EMBO J. *26*, 242–252.

Santaguida, S., and Amon, A. (2015). Short- and long-term effects of chromosome mis-segregation and aneuploidy. Nat Rev Mol Cell Biol *16*, 473–485.

Santaguida, S., Vasile, E., White, E., and Amon, A. (2015). Aneuploidy-induced cellular stresses limit autophagic degradation. Genes Dev *29*, 2010–2021.

Santaguida, S., Richardson, A., Iyer, D.R., M'Saad, O., Zasadil, L., Knouse, K.A., Wong, Y.L., Rhind, N., Desai, A., and Amon, A. (2017). Chromosome Mis-segregation Generates Cell-Cycle-Arrested Cells with

Complex Karyotypes that Are Eliminated by the Immune System. Dev Cell *41*, 638-651 e5.

Sardiello, M., Palmieri, M., di Ronza, A., Medina, D.L., Valenza, M., Gennarino, V.A., Di Malta, C., Donaudy, F., Embrione, V., Polishchuk, R.S., et al. (2009). A Gene Network Regulating Lysosomal Biogenesis and Function. Science (80-.). *325*, 473–477.

Sasaki, T., Lian, S., Khan, A., Llop, J.R., Samuelson, A. V., Chen, W., Klionsky, D.J., and Kishi, S. (2017). Autolysosome biogenesis and developmental senescence are regulated by both Spns1 and v-ATPase. Autophagy *13*, 386–403.

Sekine, Y., Hatanaka, R., Watanabe, T., Sono, N., Iemura, S., Natsume, T., Kuranaga, E., Miura, M., Takeda, K., and Ichijo, H. (2012). The Kelch repeat protein KLHDC10 regulates oxidative stress-induced ASK1 activation by suppressing PP5. Mol Cell *48*, 692–704.

Serpionov, G. V., Alexandrov, A.I., Antonenko, Y.N., and Ter-Avanesyan, M.D. (2016). A protein polymerization cascade mediates toxicity of non-pathological human huntingtin in yeast. Sci. Rep. *5*, 18407.

Shpilka, T., and Haynes, C.M. (2018). The mitochondrial UPR: mechanisms, physiological functions and implications in ageing. Nat. Rev. Mol. Cell Biol. *19*, 109–120.

Siegrist, S.E., Haque, N.S., Chen, C.H., Hay, B.A., and Hariharan, I.K. (2010). Inactivation of both Foxo and reaper promotes long-term adult neurogenesis in Drosophila. Curr Biol *20*, 643–648.

Stingele, S., Stoehr, G., and Storchova, Z. (2013). Activation of autophagy in cells with abnormal karyotype. Autophagy *9*, 246–248.

Suraweera, A., Münch, C., Hanssum, A., and Bertolotti, A. (2012). Failure of Amino Acid Homeostasis Causes Cell Death following Proteasome Inhibition. Mol. Cell *48*, 242–253.

Sykiotis, G.P., and Bohmann, D. (2008). Keap1/Nrf2 signaling regulates oxidative stress tolerance and lifespan in Drosophila. Dev Cell *14*, 76–85.

Takáts, S., Nagy, P., Varga, Á., Pircs, K., Kárpáti, M., Varga, K., Kovács, A.L., Hegedűs, K., and Juhász, G. (2013). Autophagosomal Syntaxin17-dependent lysosomal degradation maintains neuronal function in Drosophila. J. Cell Biol. *201*, 531–539.

Takeda, K., Komuro, Y., Hayakawa, T., Oguchi, H., Ishida, Y., Murakami, S., Noguchi, T., Kinoshita, H., Sekine, Y., Iemura, S. -i., et al. (2009). Mitochondrial phosphoglycerate mutase 5 uses alternate catalytic activity

as a protein serine/threonine phosphatase to activate ASK1. Proc. Natl. Acad. Sci. *106*, 12301–12305.

Tiebe, M., Lutz, M., De La Garza, A., Buechling, T., Boutros, M., and Teleman, A.A. (2015). REPTOR and REPTOR-BP Regulate Organismal Metabolism and Transcription Downstream of TORC1. Dev. Cell *33*, 272–284.

Tillberg, P.W., Chen, F., Piatkevich, K.D., Zhao, Y., Yu, C.-C., English, B.P., Gao, L., Martorell, A., Suk, H.-J., Yoshida, F., et al. (2016). Protein-retention expansion microscopy of cells and tissues labeled using standard fluorescent proteins and antibodies. Nat. Biotechnol. *34*, 987–992.

Tognon, E., Kobia, F., Busi, I., Fumagalli, A., De Masi, F., and Vaccari, T. (2016). Control of lysosomal biogenesis and Notch-dependent tissue patterning by components of the TFEB-V-ATPase axis in Drosophila melanogaster. Autophagy *12*, 499–514.

Torres, E.M., Dephoure, N., Panneerselvam, A., Tucker, C.M., Whittaker, C. a, Gygi, S.P., Dunham, M.J., and Amon, A. (2010). Identification of aneuploidy-tolerating mutations. Cell *143*, 71–83.

Uhlirova, M., and Bohmann, D. (2006). JNK- and Fos-regulated Mmp1 expression cooperates with Ras to induce invasive tumors in Drosophila. EMBO J. *25*, 5294–5304.

Wang, C.-W., Purkayastha, A., Jones, K.T., Thaker, S.K., and Banerjee, U. (2016). In vivo genetic dissection of tumor growth and the Warburg effect. Elife *5*.

Wu, H., Wang, M.C., and Bohmann, D. (2009). JNK protects Drosophila from oxidative stress by trancriptionally activating autophagy. Mech. Dev. *126*, 624–637.

Zhang, T., Zhou, Q., Ogmundsdottir, M.H., Moller, K., Siddaway, R., Larue, L., Hsing, M., Kong, S.W., Goding, C.R., Palsson, A., et al. (2015). Mitf is a master regulator of the v-ATPase, forming a control module for cellular homeostasis with v-ATPase and TORC1. J. Cell Sci. *128*, 2938–2950.

Zhu, J., Tsai, H.-J., Gordon, M.R., and Li, R. (2018). Cellular Stress Associated with Aneuploidy. Dev. Cell *44*, 420–431.

Zielke, N., Korzelius, J., van Straaten, M., Bender, K., Schuhknecht, G.F., Dutta, D., Xiang, J., and Edgar, B.A. (2014). Fly-FUCCI: A versatile tool for studying cell proliferation in complex tissues. Cell Rep *7*, 588–598.

Key Resources Table

REAGENT or RESOURCE	SOURCE	IDENTIFIER
Antibodies		
mouse anti-MMP1 (14A3D2)	Developmental Studies Hybridoma bank	RRID:AB_579782
rat anti-Ci	Developmental Studies Hybridoma bank	RRID:AB_2109711
rabbit anti-cleaved Dcp1	Cell Signaling Technology	RRID:AB_2721060
rabbit anti-PH3	Merck	Code: 06-570
mouse anti-P-H2Av (1:500);	Developmental Studies Hybridoma bank	RRID:AB_2618077
mouse anti-Ubiquitin	Enzo Life Science	RRID:AB_10541840
rabbit anti-Ref(2)P	Tor Erik Rusten, University of Oslo (Norway)	
rabbit anti-βgal	Cappel	
rabbit-anti-p-eIF2α	Cell Signaling Technology	RRID:AB_390740
Alexa fluor 488-conjugated AffiniPure Donkey Anti-Mouse IgG (H+L)	Jackson ImmunoResearch	RRID:AB_2341099
Cy2 AffiniPure Donkey Anti-Rabbit IgG (H+L)	Jackson ImmunoResearch	RRID:AB_2307385
Cy3 AffiniPure Donkey Anti-Mouse IgG (H+L)	Jackson ImmunoResearch	RRID:AB_2315777
Cy3 AffiniPure Donkey Anti-Rabbit IgG (H+L)	Jackson ImmunoResearch	RRID:AB_2307443
Cy5 AffiniPure Donkey Anti-Rat IgG (H+L)	Jackson ImmunoResearch	RRID:AB_2340671
Chemicals, Peptides and Recombinant Proteins		
Click-iT™ Plus EdU Alexa Fluor™ 647 Imaging Kit	Invitrogen	Code: C10640
CellEvent™Senescence Green detection kit	Invitrogen	Code: C10850
DAPI	Sigma Aldrich	Code: 28718-90-3
DH3	Molecular Probes	Code: D11347
Mitosox	Molecular Probes	Code: M36008
Tetramethylrhodamine ethyl ester (TMRE)	Invitrogen	Code: T669
Comet Assay Kit	Trevigen	Code: 4250-050K
In Situ Cell Death Detection Kit, Fluorescein (TUNEL)	Roche	Code:11684 795910
Acryloly-X	Thermo Fisher	Code: A20770
Experimental Models. Organisms/Strains	Vienna Drosophila Resource Center	VDRC ID_26669
en-GAL4	Bloomington Drosophila Stock Center	RRID:BDSC_1973
ap-GAL4	Bloomington Drosophila Stock Center	RRID:BDSC_3041
ey-GAL4	Bloomington Drosophila Stock Center	RRID:BDSC_5535
UAS-bub3-RNAi	Vienna Drosophila Resource Center	VDRC ID_21037
UAS-asp-RNAi	Vienna Drosophila Resource Center	VDRC ID_ 110177
UAS-gfp-RNAi	Bloomington Drosophila Stock Center	RRID:BDSC_35786
UAS-msl1-RNAi	Bloomington Drosophila Stock Center	RRID:BDSC_9239
UAS-mud-RNAi	Bloomington Drosophila Stock Center	RRID:BDSC_28074
UAS-p35	Bloomington Drosophila Stock Center	RRID:BDSC_5072 RRID:BDSC_5073
UAS-miRHG	(Siegrist et al., 2010)	N/A
UAS-myristoylated-Tomato	Bloomington Drosophila Stock Center	RRID:BDSC_32221
UAS-sip3-RNAi	Vienna Drosophila Resource Center	VDRC ID_6870

UAS-rpn1-RNAi	Bloomington Drosophila Stock Center	RRID:BDSC_34348
UAS-rpn7-RNAi	Bloomington Drosophila Stock Center	RRID:BDSC_34787
UAS-rpn11-RNAi	Bloomington Drosophila Stock Center	RRID:BDSC_33662
UAS-Htt-25Q-Cerulean	Bloomington Drosophila Stock Center	RRID:BDSC_58360
UAS-ref(2)P-RNAi	Bloomington Drosophila Stock Center	RRID:BDSC_36111
UAS-atg1-RNAi	Vienna Drosophila Resource Center	VDRC ID_13133
UAS-atg2-RNAi	Vienna Drosophila Resource Center	VDRC ID_108447
UAS-atg6-RNAi	Vienna Drosophila Resource Center	VDRC ID_110197
UAS-atg8-RNAi	Vienna Drosophila Resource Center	VDRC ID_43097
UAS-atg9-RNAi	Vienna Drosophila Resource Center	VDRC ID_10045
UAS-atg12-RNAi	Vienna Drosophila Resource Center	VDRC ID_29791
UAS-atg18-RNAi	Vienna Drosophila Resource Center	VDRC ID_22643
UAS-mitf-RNAi	Vienna Drosophila Resource Center	VDRC ID_108519
UAS-syx17-RNAi	Bloomington Drosophila Stock Center	RRID:BDSC_36595
UAS-Rheb	Bloomington Drosophila Stock Center	RRID:BDSC_9688
UAS-BiP-RNAi	Bloomington Drosophila Stock Center	RRID:BDSC_32402
UAS-spin-GFP	F. Pignoni, SUNY Upstate Medical University, Syracuse, USA	N/A
UAS-BiP	Bloomington Drosophila Stock Center	RRID:BDSC_5843
UAS-mfn-RNAi	Bloomington Drosophila Stock Center	RRID:BDSC_31157
UAS-omi-RNAi	Vienna Drosophila Resource Center	VDRC ID_24106
UAS-park-RNAi	Bloomington Drosophila Stock Center	RRID:BDSC_38333
UAS-park	Bloomington Drosophila Stock Center	RRID:BDSC_34746
UAS-spargel-RNAi	Bloomington Drosophila Stock Center	RRID:BDSC_33915
UAS-usp14-RNAi	Bloomington Drosophila Stock Center	RRID:BDSC_66956
UAS-Sod2	Bloomington Drosophila Stock Center	RRID:BDSC_24494
UAS-Cat-A	Bloomington Drosophila Stock Center	RRID:BDSC_24621
UAS-Sod2, GTPx-1	N. Perrimon, Harvard University, Boston, USA	N/A
UAS-hsp60	N. Perrimon, Harvard University, Boston, USA	N/A
UAS-hsp60c	N. Perrimon, Harvard University, Boston, USA	N/A
UAS-ref(2)P-GFP	G. Juhász, Eötvös Loránd University, Budapest, Hungary	N/A
UAS-puc2A	(Martin-Blanco et al., 1998)	N/A
UAS-bsk-DN	Bloomington Drosophila Stock Center	RRID:BDSC_6405
UAS-dap-RNAi	Bloomington Drosophila Stock Center	RRID:BDSC_64026
UAS-ask1-K618M (DN)	M. Miura, Tokyo University, Tokyo, Japan	N/A
UAS-p53-RNAi	Vienna Drosophila Resource Center	VDRC ID_38235
ub-EGFP-E2F1$^{1-230}$, ub-RFP-CycB$^{1-266}$	Bloomington Drosophila Stock Center	RRID:BDSC_55123
ub-EGFP-E2F1$^{1-230}$, ub-RFP-CycB$^{1-266}$	Bloomington Drosophila Stock Center	RRID:BDSC_55124
hid-EGFP.5'F-WT (p53-sensor)	Bloomington Drosophila Stock Center	RRID:BDSC_50750
UAS-p53-RNAi	Bloomington Drosophila Stock Center	RRID:BDSC_66956
dap-lacZ	Bloomington Drosophila Stock Center	RRID:BDSC_10406
UAS-mitoGFP	Bloomington Drosophila Stock Center	RRID:BDSC_8442
UAS-mito-mCherry	Bloomington Drosophila Stock Center	RRID:BDSC_66532
UAS-mitoTimer	Bloomington Drosophila Stock Center	RRID:BDSC_57323
UAS-mitoQC	(Lee et al., 2018)	N/A
UAS-mito-Keima	(Lee et al., 2018)	N/A
UAS-mitoGCaMP	Alex Whitworth, Medical Research Council, Cambridge, United Kingdom	N/A
UAS-GCaMP	Bloomington Drosophila Stock Center	RRID:BDSC_42748
UAS-GFP-mCherry-Atg8a	Bloomington Drosophila Stock Center	RRID:BDSC_37749
3xmCherry-Atg8a	(Hegedűs et al., 2016)	N/A

MMP1-GFP	(Uhlirova and Bohmann, 2006)	N/A
GstD-GFP	(Sykiotis and Bohmann, 2008)	N/A
UAS-CL1-GFP	(Pandey et al., 2007)	N/A
Tub-Lamp1-GFP	H. Krämer, UT Southwestern Medical Center, Dallas, USA	N/A
Tub-Lamp1-YFP	Kyoto DGRC	DGRC: 115240
HP1-RFP	Bloomington Drosophila Stock Center	RRID:BDSC_30562
Mitf-2.2-GFP	(Zhang et al., 2015)	N/A
4Mbox-GFP	(Zhang et al., 2015)	N/A
unk-GFP	(Tiebe et al., 2015)	N/A
LDH-GFP	(Wang et al., 2016)	RRID:BDSC_57323
sima-GFP	Bloomington Drosophila Stock Center	RRID:BDSC_60222
ODD-GFP	(Misra et al., 2017)	N/A
UAS-nlsDsREDFT	(Lidsky et al., 2018)	N/A
UAS-sima-RNAi	Bloomington Drosophila Stock Center	RRID:BDSC_33895RRID:BDSC_33894 RRID:BDSC_26207
UAS-Xbp1-GFP	(Ryoo et al., 2007)	N/A
UAS-TOR	Bloomington Drosophila Stock Center	RRID:BDSC_7012
PERK-GFP	Bloomington Drosophila Stock Center	RRID:BDSC_42102
ATF4-GFP	Bloomington Drosophila Stock Center	RRID:BDSC_34312
ATF6-GFP	Bloomington Drosophila Stock Center	RRID:BDSC_59432
UAS-perk-RNAi	Bloomington Drosophila Stock Center	RRID:BDSC_42499
UAS-ire1-RNAi	Bloomington Drosophila Stock Center	RRID:BDSC_66741
UAS-pgam5-RNAi	Vienna Drosophila Resource Center	VDRC ID_51657
Software and Algorithms		
Fiji	Fiji	https://fiji.sc/
Excel	Microsoft Excel 2016	N/A
GraphPad Prism 7 Project	GraphPad	RRID:SCR_002798
Imaris 9.0.1	Bitplane	RRID: SCR_007370
Black Zen Software	Zeiss	RRID: SCR_018163
ec-CLEM (Icy plugin; v 1.0.1.5)	(Paul-Gilloteaux et al., 2017)	http://icy.bioimageanalysis.org/plugin/

Figure 1

Click here to access/download;Figure;Figure 1 DEVELOPMENTAL-CELL-D-20-00802.tif

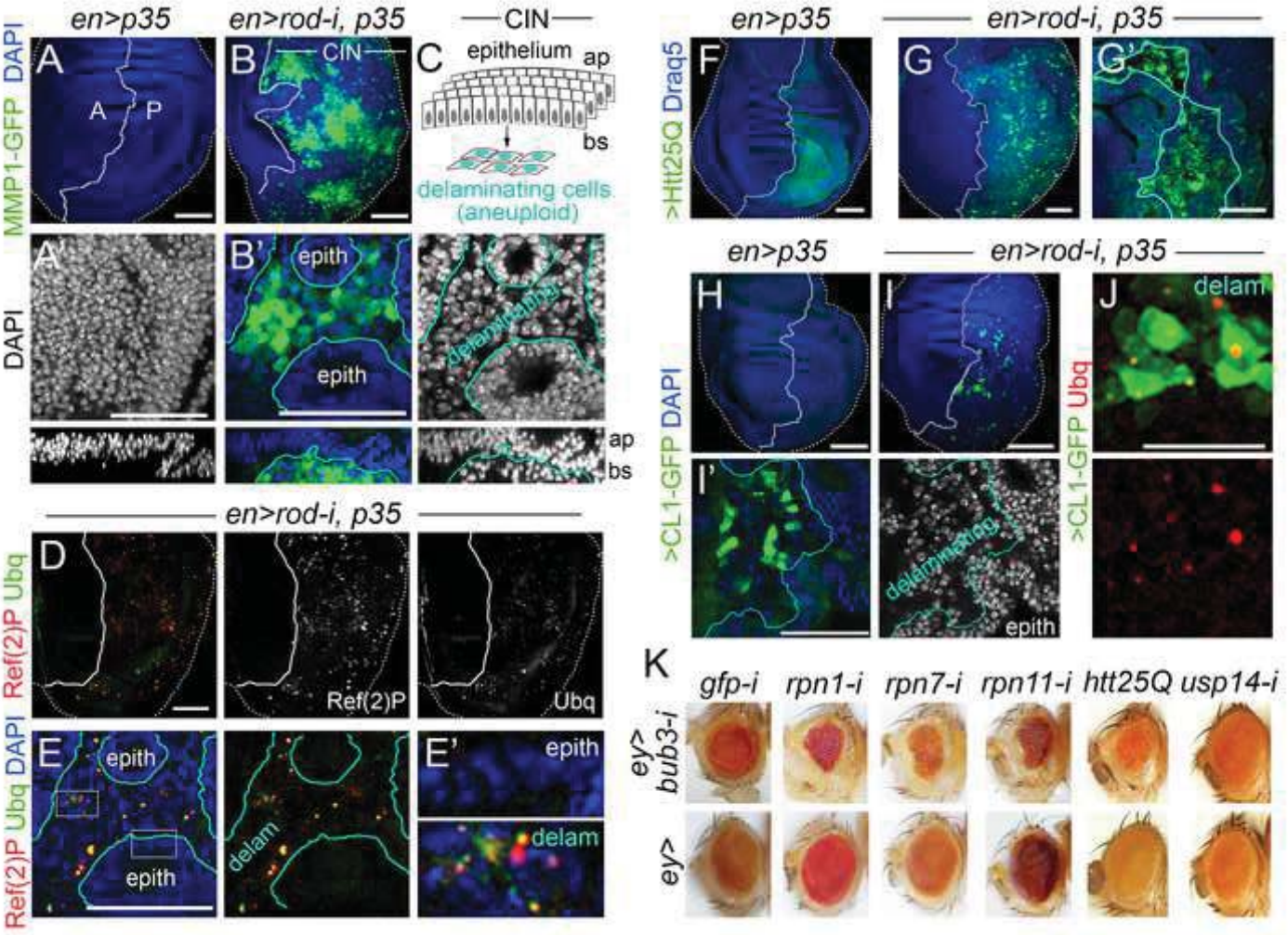

Figure 2

Click here to access/download;Figure;Figure 2 DEVELOPMENTAL-CELL-D-20-00802.tif

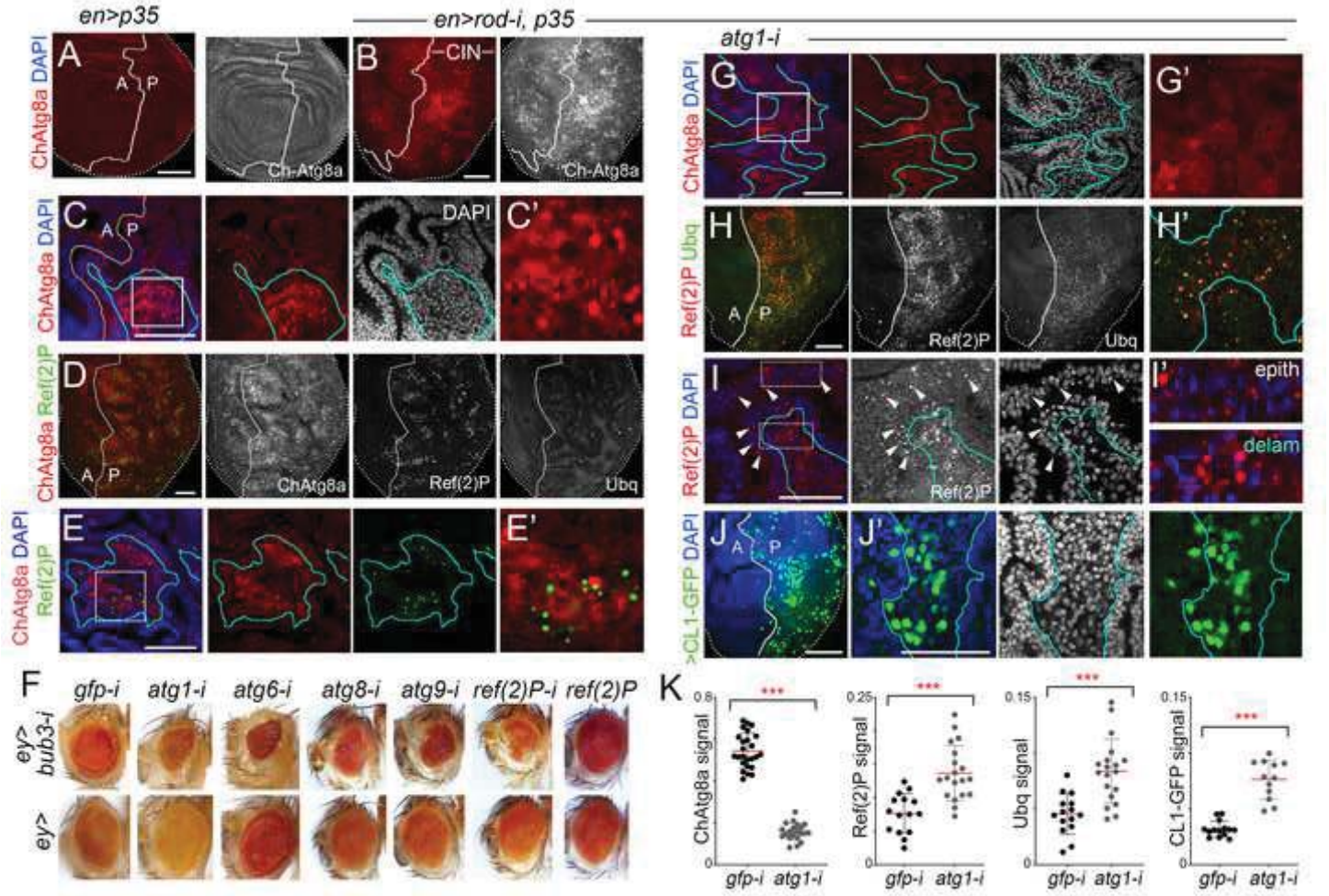

Figure 3

Click here to access/download;Figure;Figure 3 DEVELOPMENTAL-CELL-D-20-00802.tif

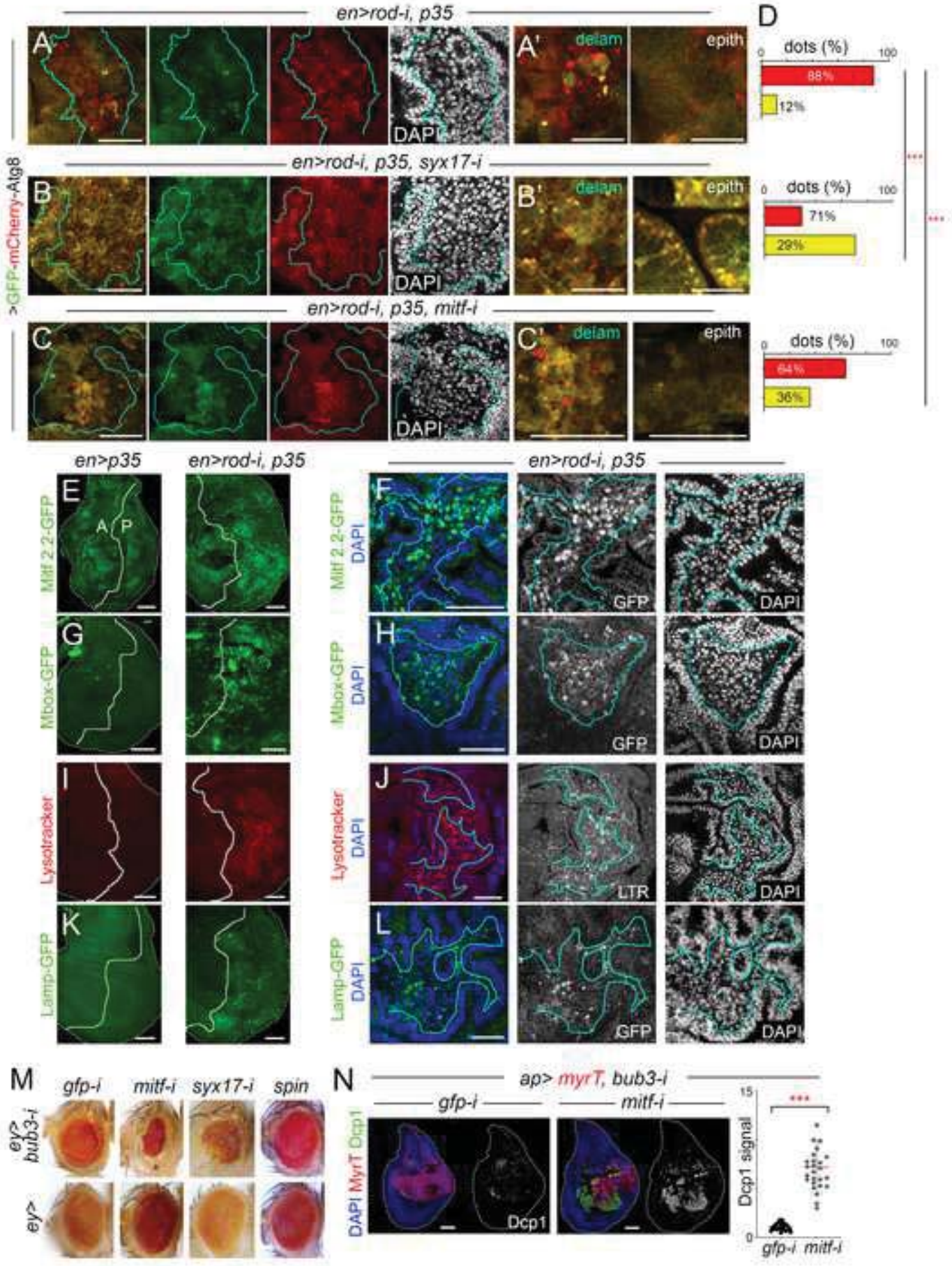

Figure 4

Click here to access/download;Figure;Figure 4 DEVELOPMENTAL-CELL-D-20-00802.tif

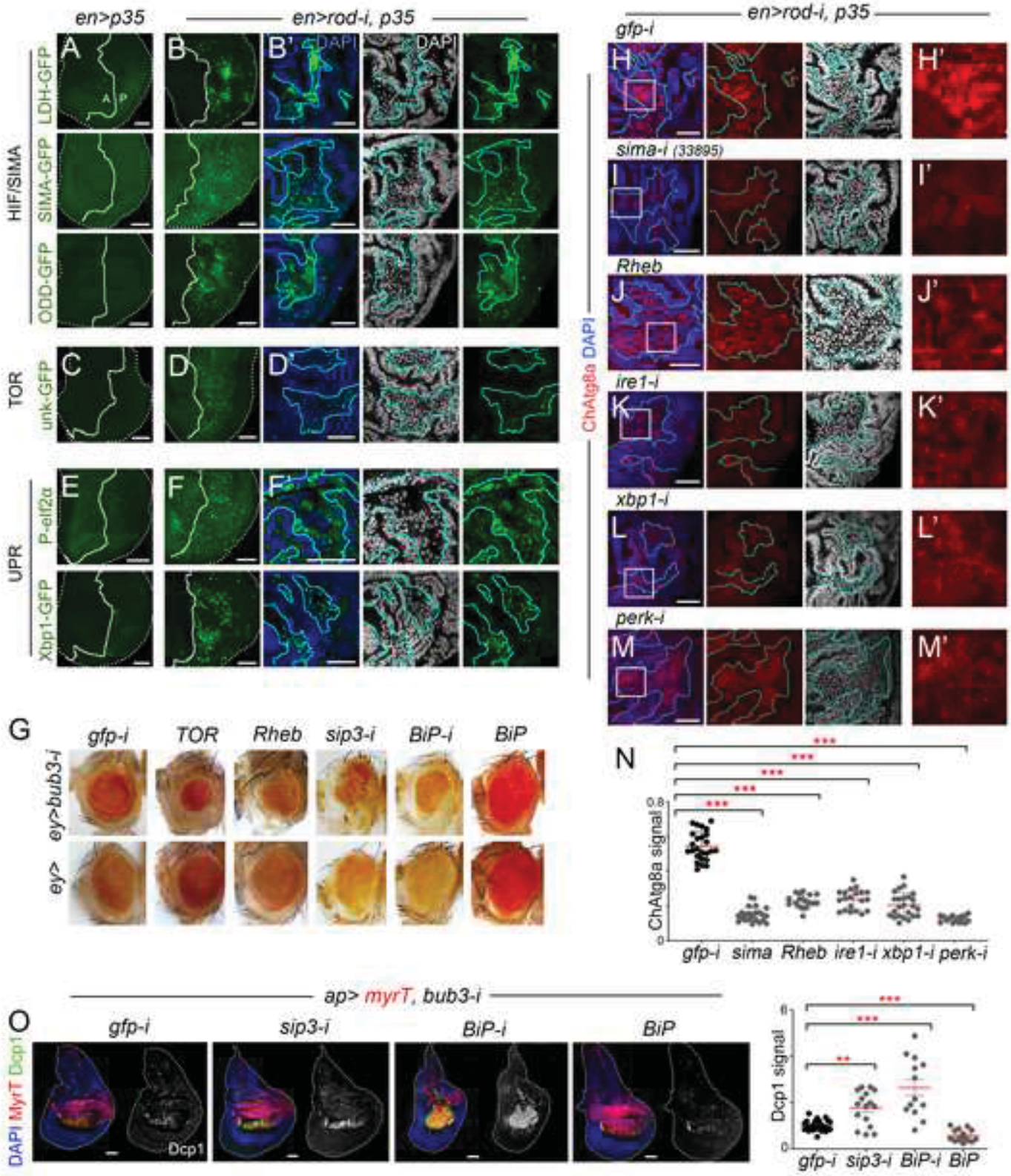

Figure 5

Click here to access/download;Figure;Figure 5 DEVELOPMENTAL-CELL-D-20-00802.tif

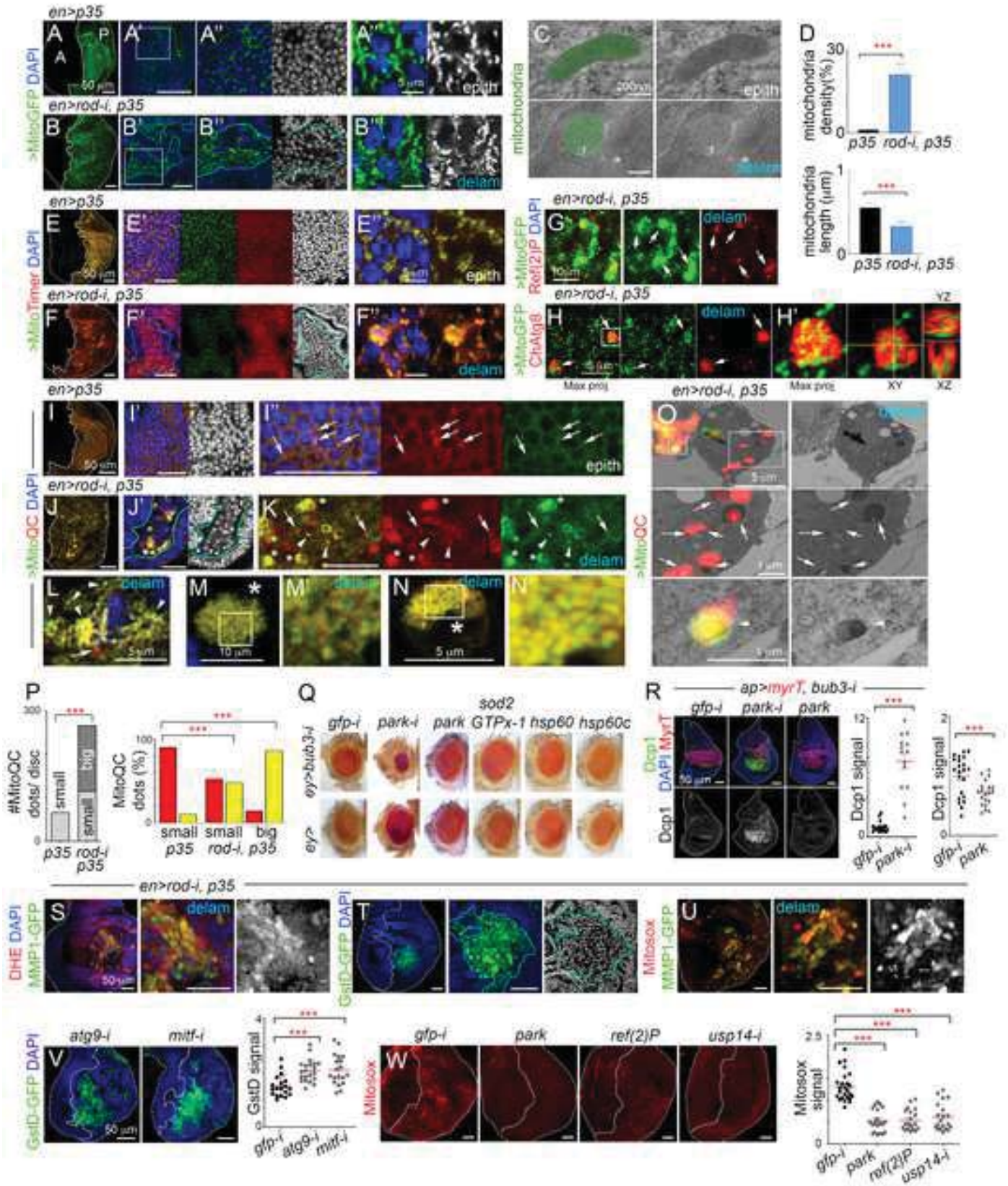

Figure 6

Click here to access/download;Figure;Figure 6 DEVELOPMENTAL-CELL-D-20-00802.tif

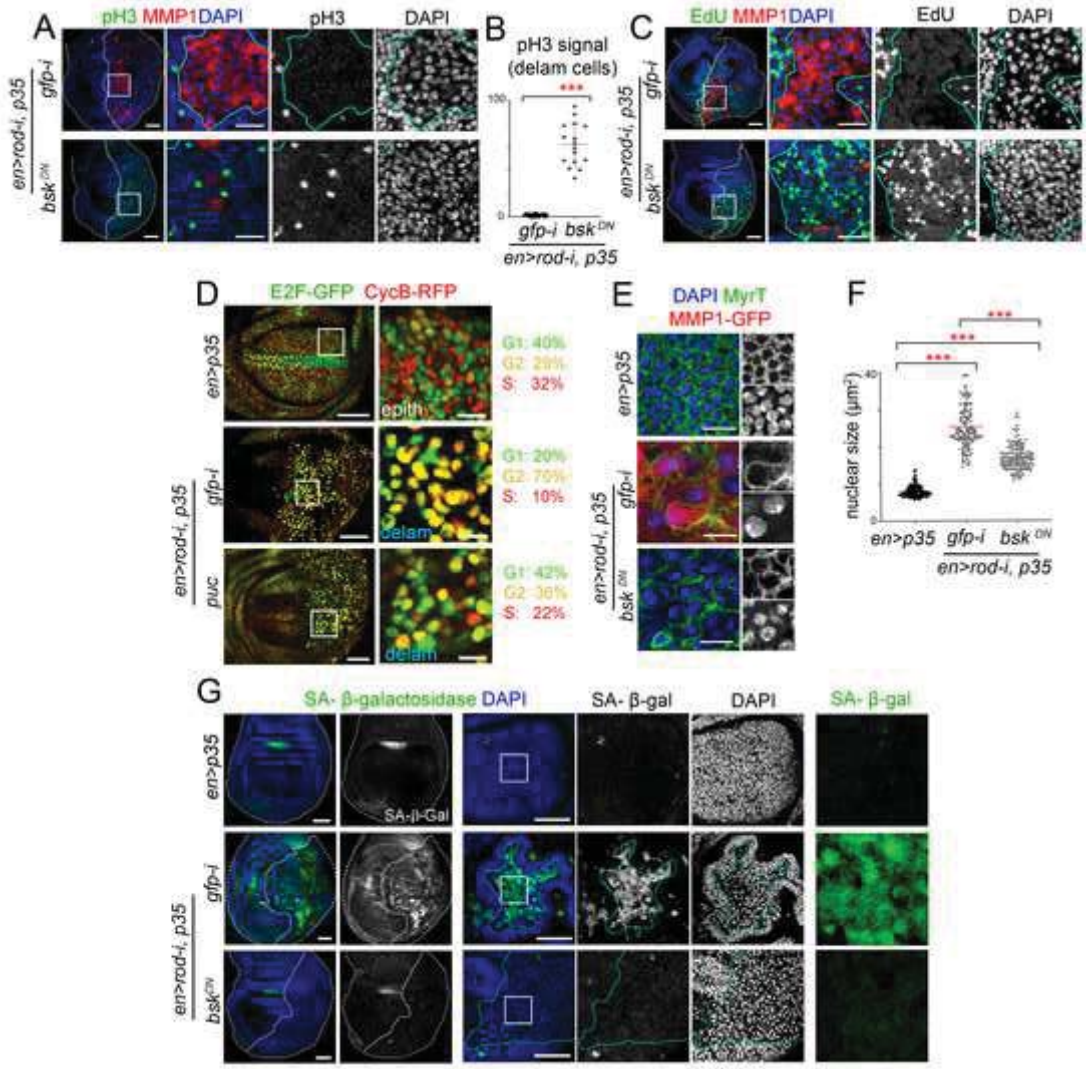

Figure 7

Click here to access/download;Figure;Figure 7 DEVELOPMENTAL-CELL-D-20-00802.tif

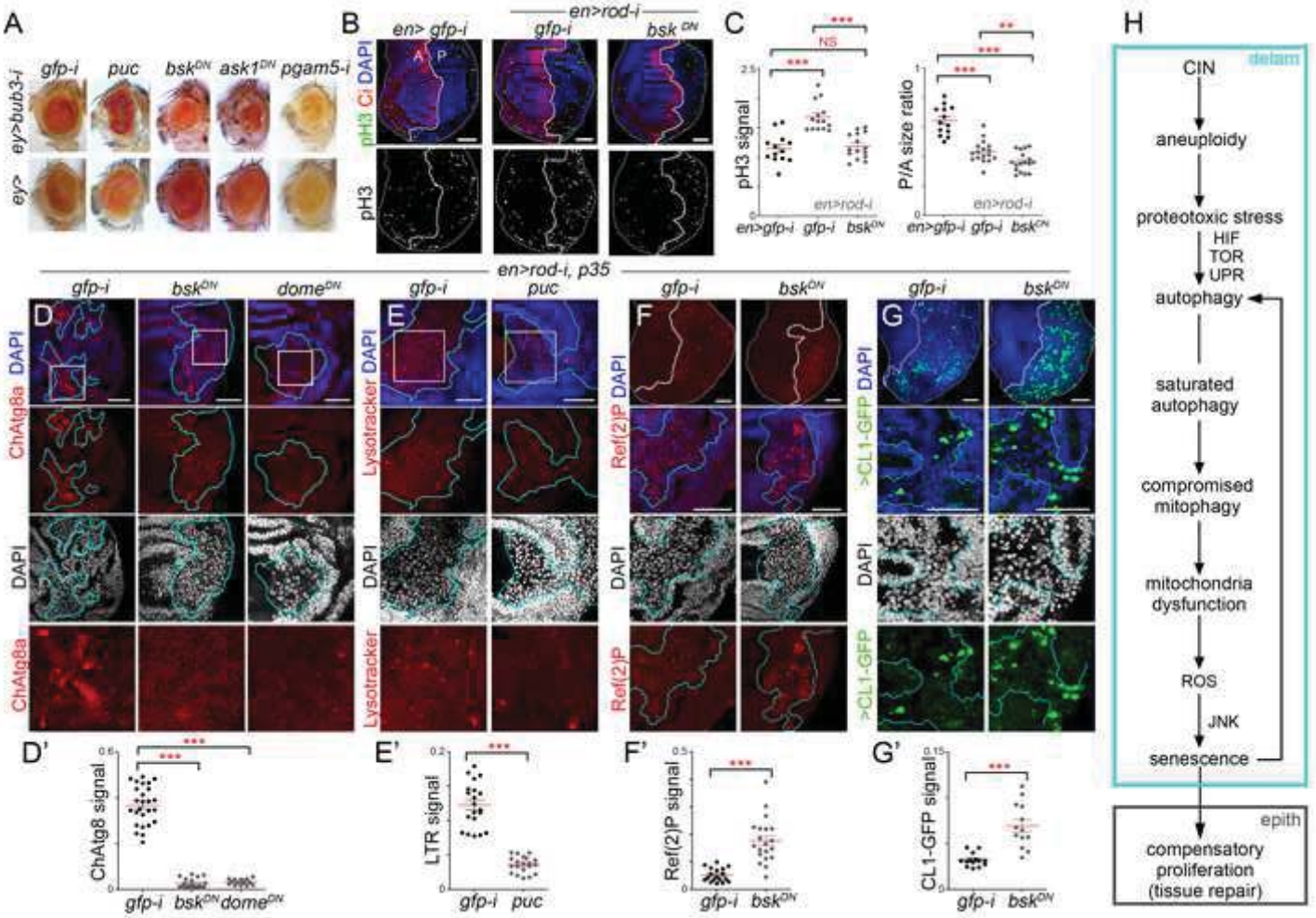

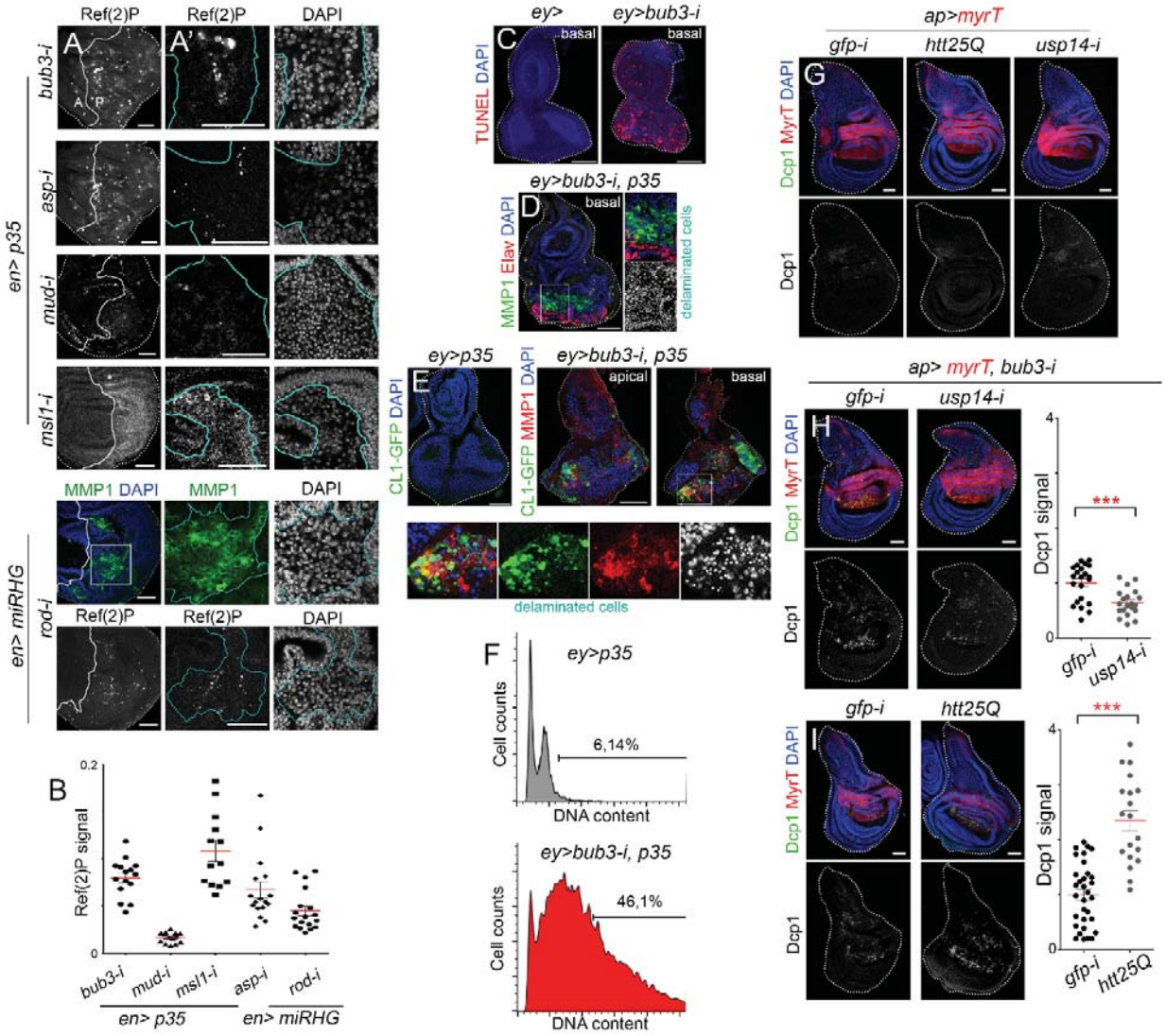

Figure S1. Proteotoxic stress is not merely a consequence of cell delamination (related to Figure 1)

(**A**, **A'**, **C-E, G-I**) Wing (**A**, **A'**, **G-I**) and eye (**C-E**) imaginal discs expressing the indicated transgenes under the control of the *en-gal4* (**A**, **A'**), *eyeless-gal4* (**C-E**), and *ap-gal4* (**G-I**) drivers and stained for Ref(2)P (white), MMP1 (green) or DAPI (white) in **A**, **A',** TUNEL (red) and DAPI (blue) in **C**, MMP1 (green), Elav (red) and DAPI (blue or white) in **D**, CL1-GFP (green), MMP1 (red) and DAPI (blue or white) in **E**, and Dcp1 (green or white), MyrT (red) and DAPI (blue) in **H-I** . Scale bars, 50 µm. (**B**, **H**, **I**) Scatter plots showing the amount of Ref(2)P (**B**) or Dcp1 (**H**, **I**) signal per area of wing discs expressing the indicated transgenes. Mean and SD are shown. Statistically significant differences based on Student's t-test are indicated. *** p<0.001. (**F**) DNA content profile of eye imaginal discs cells expressing the indicated transgenes under the control of the *eyeless-*

gal4 driver. Percentage of cells with DNA content bigger than 4C is shown, as proxy to compare aneuploidy levels.

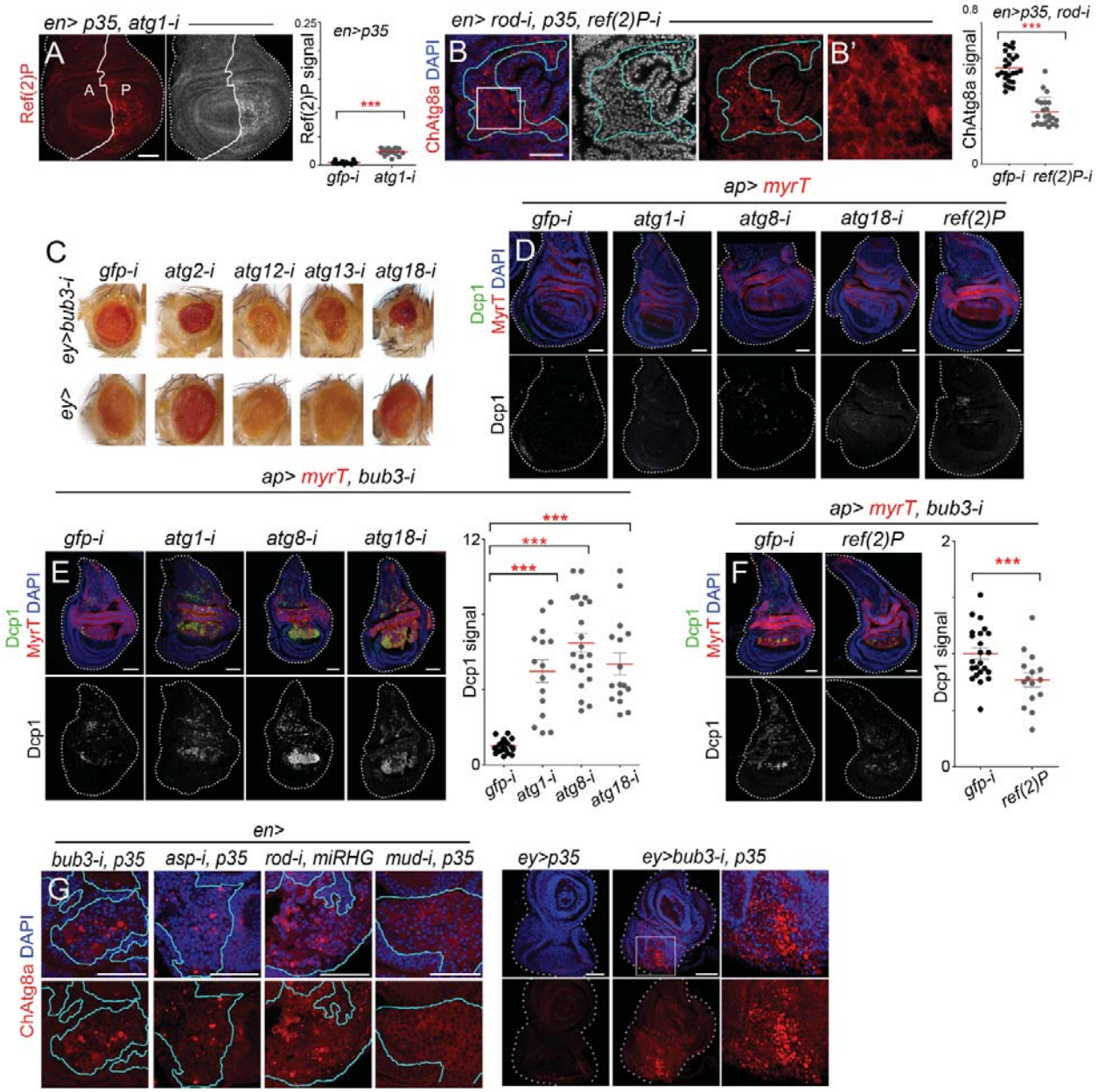

Figure S2. Autophagy contributes to dampen the deleterious effects of CIN (related to Figure 2)

(**A**-**B'**, **D**-**G**) Wing imaginal discs expressing the indicated transgenes under the control of the *en-gal4* (**A**-**B'**, **G**), *ap-gal4* (**D**-**F**) or *eyeless-gal4* (**G**) drivers, and stained for Ref(2)P (red or white, **A**), Cherry-Atg8a (ChAtg8a, red, **B**, **G**), Dcp1 (green or white, **D**-**F**), MyrT (red, **D**-**F**) and DAPI (blue or white, **B**, **D**-**G**). Right

panels in **G** are higher magnifications of the region marked with a white square in the eye imaginal disc. (**C**) Adult eyes of male individuals expressing the indicated transgenes under the control of the *ey-gal4* driver. (**A**, **B**, **E**, **F**) Scatter plots showing the amount of Ref(2)P (**A**), ChAtg8a (**B**) and Dcp1 (**E**, **F**) signal per area of wing discs expressing the indicated transgenes. Mean and SD are shown. Statistically significant differences based on Student's t-test (**A**, **B**, **F**) or Dunnett's test (**E**) are indicated. *** p<0.001. Scale bars, 50 µm.

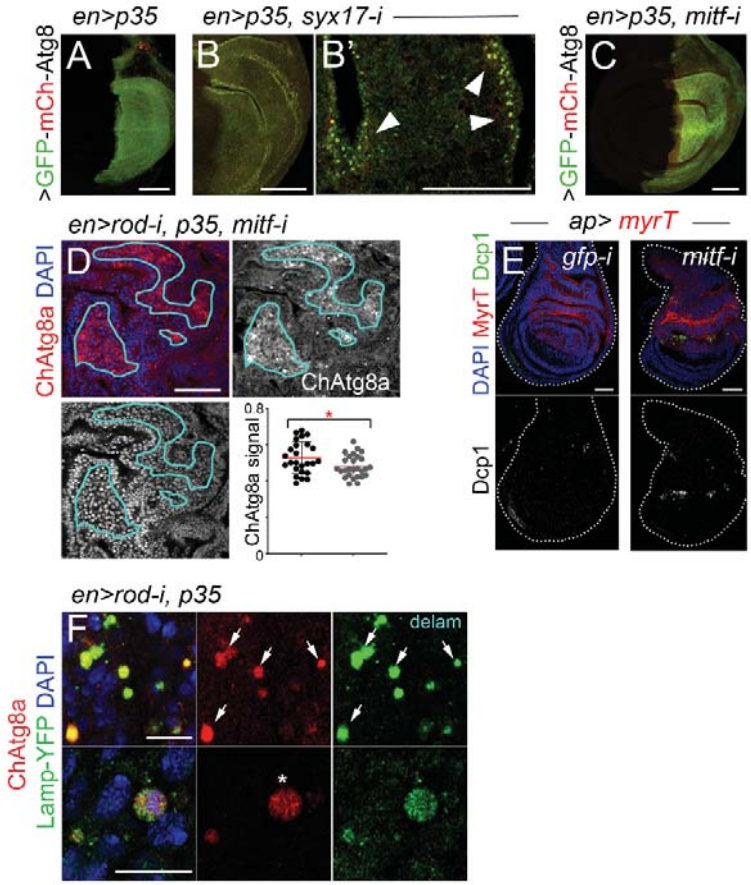

Figure S3 Autophagy flux in CIN tissues (related to Figure 3)

(**A**-**F**) Wing imaginal discs expressing the indicated transgenes under the control of the *en-gal4* (**A**-**D**, **F**) or *ap-gal4* (**E**) driver and stained for GFP-mCherry-Atg8a (green and red, **A**-**C**), Cherry-Atg8a (ChAtg8a, red or white, **D**, **F**), Dcp1 (green or white, **E**), MyrT (red, **E**), Lam-YFP (green, **F**), and DAPI (blue or white, **D**-**F**). Arrows in **F** point to ChAtg8a-positive puncta colocalizing with Lam-YFP. (**C**) Scatter plot showing the amount of ChAtg8a (**C**) signal per area of wing discs expressing the indicated transgenes. Mean and SD are shown.

Statistically significant differences based on Student's t-test are indicated. * p<0.05. Scale bars, 50 µm (**A**, **B**, **C-E**), 25 µm (**B'**), 10 µm (**F**),

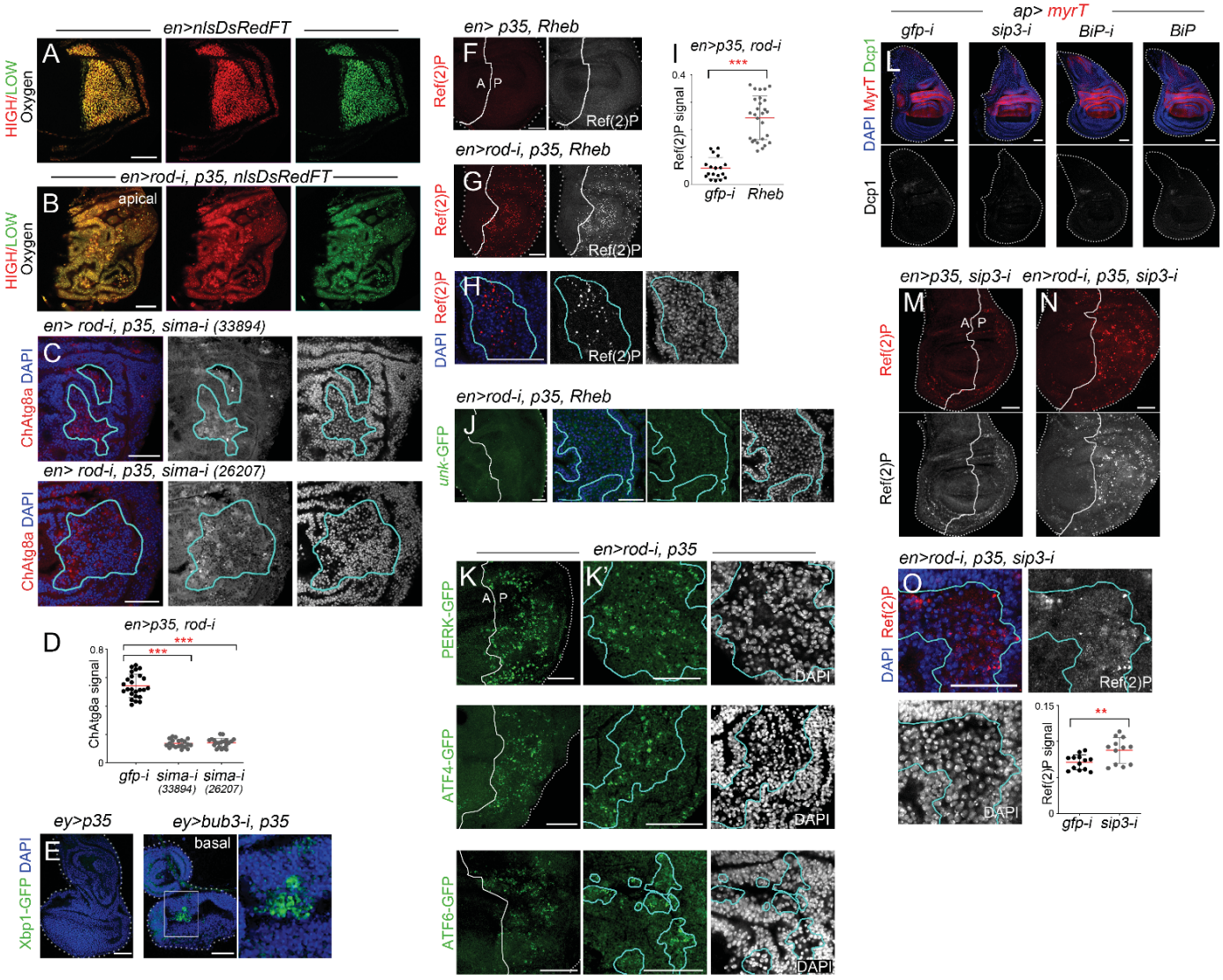

Figure S4. UPR, HIF and autophagy induction in CIN tissues (related to Figure 4)

(**A-C, E-O**) Wing (**A-C, F-O**) and eye (**E**) imaginal discs expressing the indicated transgenes under the control of the *en-gal4* (**A-C, F-K'**, **M-O**), *ey-gal4* (**E**) or *ap-gal4* (**L**) driver and stained for nlsDsRedFT (red and green, **A**, **B**, for imaging of oxygenation), Cherry-Atg8a (ChAtg8a, red or white, **C**), Xbp1-GFP (green, **E**), Ref(2)P (red or white, **F-H**, **M-O**), unk-GFP (green, **J**), PERK-GFP (green, **K**, **K'**), ATF4-GFP (green, **K**, **K'**), ATF6-GFP (green, **K**, **K'**), Dcp1 (green or white, **L**), MyrT (red, **L**) and DAPI (blue or white, **C, E, H, J-L, O**). At high oxygen levels, nlsDsRed matures predominantly into a red fluorescent isoform whereas at low oxygen levels,

a green fluorescent isoform is favored. No major difference was observed between CIN and control wing discs in **A**, **B**. (**D**, **I**, **O**) Scatter plots showing the amount of ChAtg8 (**D**) and Ref(2)P (**I**, **O**) signal per area of wing discs expressing the indicated transgenes. Mean and SD are shown. Statistically significant differences based on Dunnett's test (**D**) or Student's t-test (**I**, **O**) are indicated. ** $p<0.01$, *** $p<0.001$. Scale bars, 50 μm.

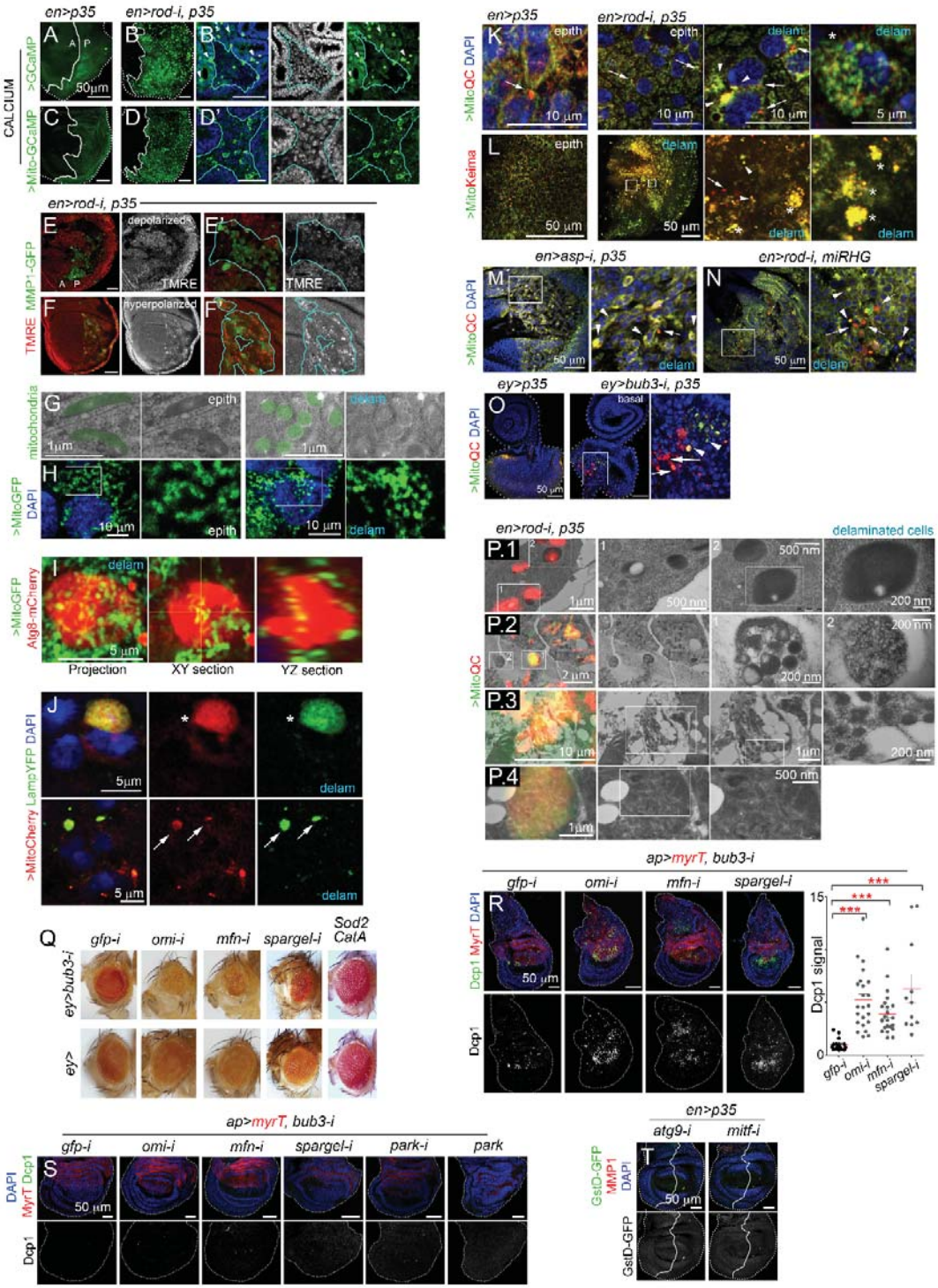

Figure S5. Mitochondrial dysfunction and ROS contribute to the deleterious effects of CIN (related to Figure 5)

(**A**-**F', H**-**O**, **R**-**T**) Wing (**A**-**F', H**-**N**, **R**-**T**) and eye (**O**) imaginal discs expressing the indicated transgenes under the control of the *en-gal4* (**A**-**F'**, **H**-**N**, **T**), *ey-gal4* (**O**), or *ap-gal4* (**R**, **S**) drivers, and stained for GCaMP (green, **A**-**B'**), Mito-GCaMP (green, **C**-**D'**), MMP1-GFP (green, **E**-**F'**), TMRE (red and white, **E**-**F'**), Mito-GFP (green, **H**, **I**), Cherry-Atg8a (red, **I**), Mito-Cherry (red, **J**), Lamp-YFP (green, **J**), Mito-QC (red and green, **K**, **M**-**O**), Mito-Keima (red and green, **L**), Dcp1 (green or white, **R**, **S**), MyrT (red, **R**, **S**), GstD-GFP (green or white, **T**), MMP1 (red, **T**) and DAPI (blue). In **J**, arrows and asterisks point to Lam-YFP-positive signal colocalizing with small MitoCherry-positive puncta or aggegates, respectively. In **K**- **O**, arrows point to red MitoQC-positive puncta, arrowheads to yellow MitoQC-positive puncta and asterisks to yellow MitoQC-positive aggregates. (**G**, **P**) TEM (**G**) and CLEM (**P**) of wing disc cells. Mitochondria are marked in green (**G)** and labeled by the expression of MitoQC (red or yellow, **P**). (**Q**) Adult eyes of male individuals expressing the indicated transgenes under the control of the *ey-gal4* driver. (**R**) Scatter plot showing the amount of Dcp1 signal per area of wing discs expressing the indicated transgenes. Mean and SD are shown. Statistically significant differences based on Dunnett's test are indicated. *** $p<0.001$.

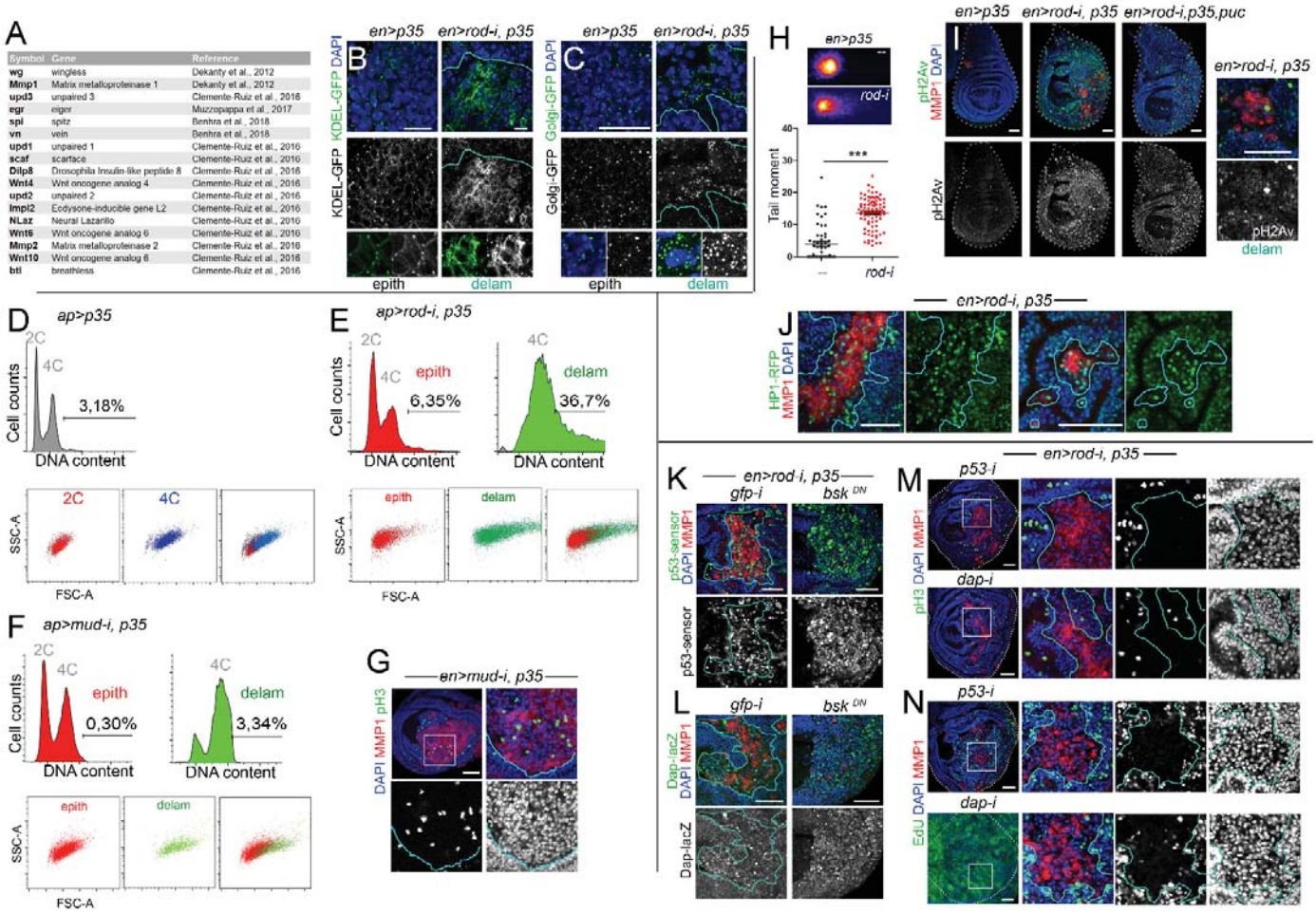

Figure S6. CIN-induced aneuploid cells enter a senescent state (related to Figure 6)

(**A**) Table of the secreted molecules expressed by the CIN-induced delaminated cells. (**B**, **C**, **G**, **I**-**N**) Wing imaginal discs expressing the indicated transgenes under the control of the *en-gal4* driver and stained for KDEL-GFP (green or white, **B**), Golgi-GFP (green or white, **C**), pH3 (green or white, **G**, **M**), MMP1 (red, **G**, **I**-**N**), pH2Av (green or white, **I**), HP1-RFP (green, **J**), p53 sensor (green or white, **K**), *dap-lacZ* (green or white, **L**), EdU (green or white, **N**) and DAPI (blue or white). Right panels in **M** and **N** are higher magnifications of the regions marked with a white square. (**D**-**F**) DNA content analysis and forward (FSC-A) and side scatter (SSC-A) density plots by fluorescence-associated cell sorter (FACS) of dorsal cells expressing the indicated transgenes under the control of the *ap-gal4* driver labeled by MyrT and MMP1-GFP. Main epithelium (MyrT-positive, GFP-negative) in red, and delaminating cells (MyrT-positive, GFP-positive) in green are shown. (**H**) Microscopy images of individual wing disc cells expressing the indicated transgenes under the control of the *en-gal4* driver and subjected to the

Comet assay. Scatter plot shows the tail moment for wing cells expressing the indicated transgenes. Each dot represents a single cell. *P*-values: Student's t-test. *** p<0.001. Scale bars, 50 µm (**G, I-N**), 20 µm (**C**), 10 µm (**B**).

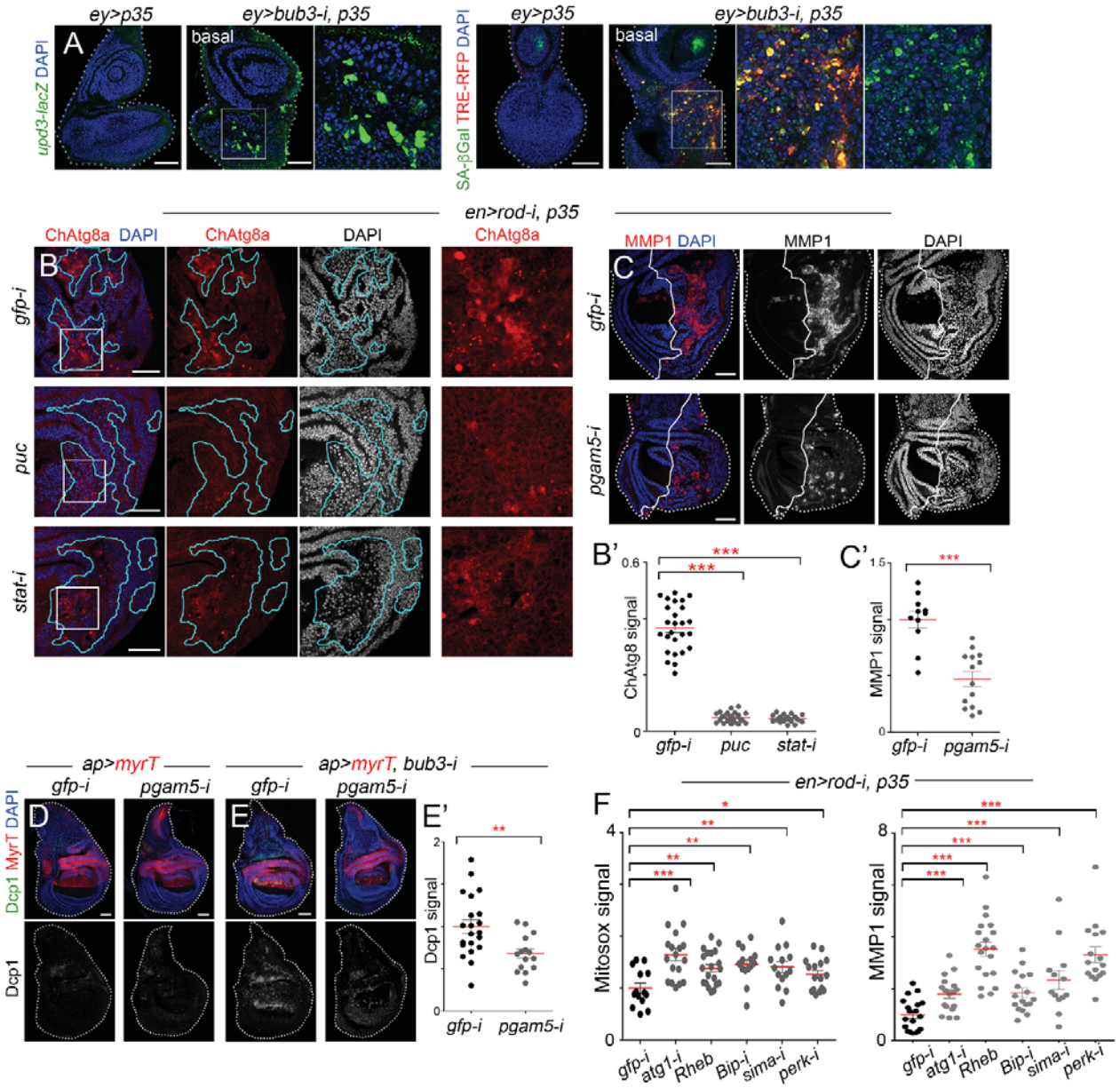

Figure S7. CIN-induced senescence contributes to proteostasis and Pgam5 to JNK activation (related to Figure 7)

(**A-C**, **D**, **E**) Eye (**A**) and wing (**B**, **C**, **D**, **E**) imaginal discs of larvae expressing the indicated transgenes under the control of the *ey-gal4* (**A**), *en-gal4* (**B**, **C**) or the *ap-gal4* (**D, E**) drivers and stained for upd3-lacZ (green),

senescence-associated (SA) β-galactosidase (green), TRE-RFP (red) and DAPI (blue) in **A**, Cherry-Atg8a (ChAtg8a, red, **B**), MMP1 (red or white, **C**), Dcp1 (green or white, **D**, **E**), MyrT(red, **D**, **D**) and DAPI (blue or white). Right panels in **B** are higher magnifications of the regions marked with a white square in the wing discs shown in upper panels. (**B'**, **C'**, **E'**, **F**) Scatter plots showing the amount of ChAtg8 signal (**B'**), MMP1 (**C'**, **F**), Dcp1 (**D'**) and Mitosox (**F**) signal per area of wing discs expressing the indicated transgenes. Mean values and SD are shown. Statistically significant differences based on Dunnett's test (**B'**, **F**) or Student's t-test (**C'**, **E'**) are indicated. ** $p<0.01$, *** $p<0.001$. Scale bars, 50 μm.

genotype	stock#	figure	*n* total eyes		*ey>* phenotype	*ey>bub3-i* phenotype			interaction
			ey>	*ey>bub3-i*	wt (%)	wt (%)	mild (%)	strong (%)	
gfp-i (A)		**1**	**52**	**146**	**100**	**0**	**72,6**	**27,4**	**--**
rpn1-i	BDSC 34348	1	26	54	100	0	37,0	63,0	*enhance*
rpn7-i	BDSC 34787	1	24	50	100	0	24,0	76,0	*enhance*
rpn11-i	BDSC 33662	1	35	60	100	0	30,0	70,0	*enhance*
gfp-i (B)			**55**	**124**	**100**	**0**	**66,9**	**33,1**	**--**
Htt25Q	BDSC 58360	**1**	50	68	100	0	8,8	91,2	*enhance*
usp14-i	BDSC 66956	1	50	160	100	13,8	61,3	25,0	*rescue*
gfp-i (A)		**2**	**52**	**146**	**100**	**0**	**72,6**	**27,4**	**--**
atg1-i	VDRC 16133	2	32	80	100	0	12,5	87,5	*enhance*
atg6-i	VDRC 110197	2	56	114	100	0	22,8	77,2	*enhance*
atg2-i	VDRC 108447	Ext. data 2	36	60	100	0	0,0	100,0	*enhance*
atg12-i	atg12-i	Ext. data 2	31	66	100	0	0,0	100,0	*enhance*
atg13-i	VDRC 27955	Ext. data 2	41	64	100	0	23,4	76,6	*enhance*
gfp-i (C)			**61**	**178**	**100**	**0**	**67,4**	**32,6**	**--**
atg8-i	VDRC 43097	2	58	60	100	0	15,0	85,0	*enhance*
atg18-i	VDRC 22643	Ext. data 2	32	50	100	0	38,0	62,0	*enhance*
atg9-i	VDRC 10045	2	58	110	100	0	12,7	87,3	*enhance*
ref(2)P-i	BDSC 36111	2	41	48	100	0	12,5	87,5	*enhance*
gfp-i (B)			**55**	**124**	**100**	**0**	**66,9**	**33,1**	**--**
UAS-Ref(2)P-GFP	G. Juhász	2	50	114	100	22,8	58,8	18,4	*rescue*
gfp-i (A)		**3**	**52**	**146**	**100**	**0**	**72,6**	**27,4**	**--**
mitf-i	VDRC 108519	3	40	100	100	0	19,0	81,0	*enhance*
syx17-i	BDSC 36595	3	40	52	100	0	0,0	100,0	*enhance*
spin-GFP	F. Pignoni	3	50	149	100	19,5	57,7	22,8	*rescue*
gfp-i (A)		**4**	**52**	**146**	**100**	**0**	**72,6**	**27,4**	**--**
TOR	BDSC 7012	4	31	60	100	0	20,0	80,0	*enhance*
Rheb	BDSC 9688	4	46	54	100	0	0,0	100,0	*enhance*
sip3-i	VDRC 6870	4	53	148	100	0	15,5	84,5	*enhance*
gfp-i (D)			**--**	**98**	**100**	**0**	**71,4**	**28,6**	--
BiP-i	BDSC 32402	4	19	52	100	0	21,2	**78,8**	*enhance*
gfp-i (B)			**55**	**124**	**100**	**0**	**66,9**	**33,1**	**--**
UAS-BiP	BDSC 5843	4	50	198	100	19,2	59,1	21,7	*rescue*
gfp-i (C)		**5**	**61**	178	100	0	67,4	32,6	--
omi-i	VDRC 24106	Ext. data 5	43	88	100	0	17,0	83,0	*enhance*
mfn-i	BDSC 31157	Ext. data 5	57	31	100	0	0,0	100,0	*enhance*
spargel-i	BDSC 33915	Ext. data 5	66	137	100	0	41,6	58,4	*enhance*
park-i	BDSC 38333	5	37	134	100	0	37,3	62,7	*enhance*
gfp-i (B)			**55**	124	100	0	66,9	33,1	**--**
park	BDSC 34746	5	38	144	100	25	54,2	20,8	*rescue*
sod2,GTPx-1	N. Perrimon	5	50	132	100	24,2	56,1	19,7	*rescue*
Sod2,CatA	BDSC 24494,24621	Ext. data 5	50	108	100	27,8	55,6	16,7	*rescue*
hsp60	N. Perrimon	5	50	87	100	14,9	60,9	24,1	*rescue*
hsp60c	N. Perrimon	5	50	192	100	11,5	63,0	25,5	*rescue*
gfp-i (E)			**--**	182	100	0	66,5	33,5	**--**
UAS-puc	E. Martin-Blanco	7	40	94	100	0	44,7	55,3	*enhance*
pgam5-i	VDRC 51657	7	42	118	100	0	20,3	79,7	*enhance*
gfp-i (F)			--	124	100	0	66,9	33,1	**--**
UAS-bsk-DN	BDSC 6405	7	50	100	100	0	40,0	60,0	*enhance*
UAS-ask-DN	M. Miura	7	50	112	100	0	42,9	57,1	*enhance*

Summary ey>bub3,gfp-i								
A				146		0	72,6	27,4
B				124		0	66,9	33,1
C				178		0	67,4	32,6
D				98		0	71,4	28,6
E				182		0	66,5	33,5
F				124		0	66,9	33,1
					Average	**0**	**69**	**31**
					enhance			*>55*
					rescue	*>5*		*<25*

Table S1. Quantifications of CIN-induced eye phenotypes (related to Figure 1, 2, 3, 4, 5, 7, S2 and S5)

Table containing the transgenes (name and origin) used, the figure where they appear, the total number (n) of eyes scored and the frequency (in %) of the different phenotypes observed (wild-type, mild and strong phenotype).

Figure	Parameter	n value (wd=wing discs)	mean ± SD	p value	Statistical test
2 K	ChAtg8a	*gfp-i* : 25 wd	0,5439 ± 0,0833		
		atg1-i : 21 wd	0,0157 ± 0,0040	3,28E-23	Student's t-test
	Ref(2)P	*gfp-i* : 15 wd	0,0766 ± 0,294		
		atg1- i: 19 wd	0,1369 ± 0,0412	3,72E-05	Student's t-test
	Ubq	*gfp-i* : 15 wd	0,0452 ± 0,0181		
		atg1- i: 19 wd	0,0837 ± 0,0289	8,25E-05	Student's t-test
	CL1-GFP	*gfp-i* : 14 wd	0,0320 ± 0,0072		
		atg1- i: 12 wd	0,0763 ± 0,0174	6,73E-09	Student's t-test
3 D	GFP-mCherry-Atg8	*ctrl* : 5 wd, 13 images, 2619 dots	178 ± 64 (red) / 24 ± 9,2 (yellow)		Chi-square
		syx17-i : 6 wd, 12 images, 2713 dots	65 ± 20,4 (red) / 161 ± 32,6 (yellow)	< 0,0001	Chi-square
		mitf-i : 7 wd, 14 images, 3196 dots	143 ± 23,8 (red) / 82 ± 26,7 (yellow)	< 0,0001	Chi-square
3 N	Dcp1	*gfp-i* : 24 wd	1 ± 0,339		
		mitf-i : 26 wd	7 ± 2,4731	4,69802E-15	Student's t-test
4 N	ChAtg8a	*gfp-i* : 25 wd	0,5439 ± 0,0833		
		sima-i (33895) : 23 wd	0,15495± 0,0425	< 2,22E-16	Dunnett's test
		Rheb : 18 wd	0,2272 ± 0,0377	< 2,22E-16	Dunnett's test
		ire1-i : 20 wd	0,2355 ± 0,0571	< 2,22E-16	Dunnett's test
		xbp1-i : 24 wd	0,2041 ± 0,0703	< 2,22E-16	Dunnett's test
		perk-i : 16 wd	0,1243 ± 0,0194	< 2,22E-16	Dunnett's test
4 O	Dcp1	*gfp-i* : 23 wd	1 ± 0,24		
		sip3-i : 16 wd	1,76 ± 0,74	3,44E-03	Dunnett's test
		BiP-i : 13 wd	2,64 ± 1,28	8,96E-07	Dunnett's test
		BiP : 15 wd	0,57 ± 0,26	1,16E-04	Dunnett's test
5 D	mitochondria density	*p35* : 3 wd	1,188 ± 0,153		
		p35, rod-i : 3wd	21,037 ± 3,962	9,74E-04	Student's t-test
	mitochondria length	*p35* : 5 wd	0,559 ± 0,047		
		p35, rod-i : 5 wd	0,335 ± 0,049	8,12E-05	Student's t-test
5 P	MitoQC	*p35* : 3 wd, 6 images, 400 small dots	60 ± 6,2 (red) / 6 ± 2,3 (yellow)		Chi-square
		p35, rod-i : 4 wd, 7 images, 808 small dots	60 ± 32,5 (red) / 55 ± 17,1 (yellow)	< 0,0001	Chi-square
		p35, rod- i: 4 wd, 7 images, 1056 big dots	22 ± 7,9 (red) / 129 ± 50,7 (yellow)	< 0,0001	Chi-square
5 R	Dcp1	*gfp-i: 18 wd*	1 ± 0,54		
		park-i : 14 wd	7,83 ± 3,27	9,27E-10	Student's t-test
		gfp-i : 22 wd	1 ± 0,34		
		park : 20 wd	0,71 ± 0,21	2,34E-03	Student's t-test
5 V	GstD-GFP	*gfp-i* : 19 wd	1,504 ± 0,393		
		atg9-i : 21 wd	2,077 ± 0,418	6,92E-05	Dunnett's test
		mitf-i : 19 wd	2,105 ± 0,557	1,10E-04	Dunnett's test
5 W	Mitosox	*gfp-i* : 25 wd	1,313 ± 0,336		
		park : 21 wd	0,524 ± 0,253	3,69E-08	Dunnett's test
		ref(2)P : 20 wd	0,540 ± 0,27	3,16E-06	Dunnett's test
		usp14-i : 20 wd	0,615 ± 0,313	8,46E-05	Dunnett's test
6 B	pH3	*gfp-i* : 19 wd	1,41 ± 0,93		
		bsk-DN : 16 wd	61,78 ±18,29	8,63E-16	Student's t-test
6 F	nuclear size	*ctrl* : 6 wd, 151 nuclei	8,0974 ± 1,5366	2,22E-16 (*ctrl* vs *gfp-i*)	Turkey's test
		gfp-i : 6 wd, 165 nuclei	25,1594 ± 5,8044	2,22E-16 (*gfp-i* vs *bsk-DN*)	Turkey's test
		bsk-DN : 7 wd, 155 nuclei	16,7039 ± 3,5229	2,22E-16 (*ctrl* vs *bsk-DN*)	Turkey's test
7 C	pH3	*ctrl* : 13 wd	1,1444 ± 0,2470	2,62E-06 (*ctrl* vs *gfp-i*)	Turkey's test
		gfp-i : 14 wd	1,6784 ± 0,2456	1,16E-05 (*gfp-i* vs *bsk-DN*)	Turkey's test
		bsk-DN : 15 wd	1,1845 ± 0,2129	0,8209 (*ctrl* vs *bsk-DN*)	Turkey's test
	P/A ratio	*ctrl* : 13 wd	0,6352 ± 0,1045	1,39E-07 (*ctrl* vs *gfp-i*)	Turkey's test
		gfp-i : 17wd	0,4318 ± 0,0736	0,0128 (*gfp-i* vs *bsk-DN*)	Turkey's test
		bsk-DN : 17wd	0,3634 ± 0,0673	2,63E-12 (*ctrl* vs *bsk-DN*)	Turkey's test
7 D'	ChAtg8a	*gfp-i* : 26 wd	0,3673 ± 0,0844		
		bsk-DN : 20 wd	0,0267 ± 0,0202	< 2,22E-16	Dunnett's test
		dome-DN : 15 wd	0,0328 ± 0,0129	< 2,22E-16	Dunnett's test
7 E'	LTR	*gfp-i* : 20 wd	0,1225 ± 0,0328		
		puc : 20 wd	0,0359 ± 0,0117	1,62E-12	Student's t-test
7 F'	Ref(2)P	*gfp-i* : 18 wd	0,0520 ± 0,0246		
		bsk-DN : 20 wd	0,1770 ± 0,0813	6,98E-07	Student's t-test
7 F'	CL1-GFP	*gfp-i* : 14 wd	0,0319 ± 0,0071		
		bsk-DN : 13 wd	0,0693 ± 0,0243	1,01E-05	Student's t-test

S1 B	Ref(2)P	*bub3-i* : 15 wd	0,080 ±0,020		
		mud-i : 14 wd	0,017 ±0,006	n/a	n/a
		msl1-i : 13 wd	0,108 ±0,039	n/a	n/a
		asp-i : 17 wd	0,067 ±0,036	n/a	n/a
		rod-i : 18 wd	0,046 ±0,021	n/a	n/a
S1 H	Dcp1	*gfp-i* : 22 wd	1 ±0,33		
		usp14-i : 20 wd	0,64 ±0,24	3,03E-04	Student's t-test
S1 I	Dcp1	*gfp-i* : 32 wd	1 ±0,57		
		htt25Q : 19 wd	2,34 ±0,78	5,91E-09	Student's t-test
S2 A	Ref(2)P	*gfp-i* : 11 wd	0,005 ±0,003		
		atg1-i : 15 wd	0,023 ±0,006	3,45E-09	Student's t-test
S2 B'	ChAtg8a	gfp-i: 25 wd	1,0138 ±0,0083		
		ref(2)P-i: 22 wd	0,0296 ±0,0082	2,38409E-13	Student's t-test
S2 E	Dcp1	*gfp-i* : 24 wd	1 ±0,33		
		atg1-i : 15 wd	4,97 ±2,32	<2,22E-16	Dunnett's test
		atg8-i : 21 wd	6,49 ±2,31	<2,22E-16	Dunnett's test
		atg18-i : 16 wd	5,36 ±2,33	<2,22E-16	Dunnett's test
S2 F	Dcp1	*gfp-i* : 23 wd	1 ±0,24		
		ref(2)P : 15 wd	0,77 ±0,24	6,05E-03	Student's t-test
S3 D	ChAtg8a	*gfp-i* : 25 wd	1,0138 ±0,0083		
		mitf-i : 24 wd	0,0505 ±0,0055	0,02738485	Student's t-test
S4 D	ChAtg8a	*gfp-i* : 25 wd	0,528 ±0,085		
		sima-i(33894) : 20 wd	0,137 ±0,028	<2,22E-16	Dunnett's test
		sima-i(26207) : 20 wd	0,142 ±0,031	<2,22E-16	Dunnett's test
S4 I	Ref(2)P	*gfp-i: 18 wd*	0,0587 ±0,0392		
		Rheb : 27 wd	0,2432 ±0,0796	1,40E-11	Student's t-test
S4 O	Ref(2)P	*gfp-i* : 13 wd	0,07 ±0,01		
		sip3-i : 12 wd	0,087 ±0,018	0,008736368	Student's t-test
S5 R	Dcp1	*gfp-i* : 18 wd	1 ±0,53		
		omi-i : 23 wd	5,22 ±2,79	6,69E-09	Dunnett's test
		mfn-i : 23 wd	3,92 ±1,96	2,46E-08	Dunnett's test
		spargel-i : 11 wd	6,33 ±4,48	1,05E-08	Dunnett's test
S6 H	Tail moment	*ctrl* : 56 nuclei	3,9048 ±5,5205		
		rod-i : 87 nuclei	13,6167 ±4,8027	4,92E-21	Student's t-test
S7 B'	ChAtg8a	*gfp-i* : 26 wd	0,367 ±0.084		
		puc : 24 wd	0,049 ±0.017	<2,22E-16	Dunnett's test
		stat-i : 22 wd	0,044 ±0.017	<2,22E-16	Dunnett's test
S7 C'	MMP1	*gfp-i* : 11 wd	1 ±0,23		
		pgam5-i : 14 wd	0,46 ±0,23	8,74E-06	Student's t-test
S7 E'	Dcp1	*gfp-i* : 32 wd	1 ±0,57		
		pgam5- i: 23 wd	0,63 ±0,22	0,0055	Student's t-test
S7 F	Mitosox	*gfp-i* : 14 wd	1,00 ±0,35		
		atg1-i : 18 wd	1,64 ±0,51	1,11E-05	Dunnett's test
		Rheb : 20 wd	1,38 ±0,32	2,52E-03	Dunnett's test
		BiP-i : 14 wd	1,46 ±0,33	1,32E-03	Dunnett's test
		sima-i : 14 wd	1,41 ±0,40	5,22E-03	Dunnett's test
		perk-i : 16 wd	1,26 ±0,31	4,87E-02	Dunnett's test
	MMP1	*gfp-i* : 19 wd	1 ±0,61		
		atg1-i : 17 wd	1,79 ±0,68	1,03E-04	Dunnett's test
		Rheb : 20 wd	3,51 ±1,21	1,19E-14	Dunnett's test
		BiP-i : 13 wd	2,33 ±1,31	4,51E-06	Dunnett's test
		sima-i : 17 wd	1,84 ±0,75	6,35E-05	Dunnett's test
		perk-i : 16 wd	3,31 ±1,20	5,11E-12	Dunnett's test

Table S2. Summary of n and p-values (related to Figures 2-7 and S1-S7).

Table containing the parameters that have been quantified, the figures where these quantifications are shown, and the statistical details.

Supplemental Video 1

Click here to access/download

Supplemental Videos and Spreadsheets

Video S1 DEVELOPMENTAL-CELL-D-20-00802.mp4

Supplemental Video 2

Supplemental Video 3

Click here to access/download

Supplemental Videos and Spreadsheets

Video S3 DEVELOPMENTAL-CELL-D-20-00802.mp4

Supplemental Video 4

Click here to access/download

Supplemental Videos and Spreadsheets

Video S4 DEVELOPMENTAL-CELL-D-20-00802.mp4

Supplemental Video 5

Click here to access/download

Supplemental Videos and Spreadsheets

Video S5 DEVELOPMENTAL-CELL-D-20-00802.mp4

Supplemental Video 6

Click here to access/download

Supplemental Videos and Spreadsheets

Video S6 DEVELOPMENTAL-CELL-D-20-00802.mp4